

**AEDC-TR-95-16**

C.2

TECHNICAL REPORTS  
FULL COPY

**Application of a Modified Dynamic Compression  
System Model to a Low-Aspect-Ratio Fan:  
Effects of Inlet Distortion**

Kimball A. Shahrokhi  
Sverdrup Technology, Inc., AEDC Group

**August 1995**

**Final Report for Period October 1, 1993 — April 14, 1995**

**PROPERTY OF U.S. AIR FORCE  
AEDC TECHNICAL LIBRARY**

Approved for public release; distribution is unlimited.

**ARNOLD ENGINEERING DEVELOPMENT CENTER  
ARNOLD AIR FORCE BASE, TENNESSEE  
AIR FORCE MATERIEL COMMAND  
UNITED STATES AIR FORCE**

## NOTICES

When U. S. Government drawings, specifications, or other data are used for any purpose other than a definitely related Government procurement operation, the Government thereby incurs no responsibility nor any obligation whatsoever, and the fact that the Government may have formulated, furnished, or in any way supplied the said drawings, specifications, or other data, is not to be regarded by implication or otherwise, or in any manner licensing the holder or any other person or corporation, or conveying any rights or permission to manufacture, use, or sell any patented invention that may in any way be related thereto.

Qualified users may obtain copies of this report from the Defense Technical Information Center.

References to named commercial products in this report are not to be considered in any sense as an endorsement of the product by the United States Air Force or the Government.

This report has been reviewed by the Office of Public Affairs (PA) and is releasable to the National Technical Information Service (NTIS). At NTIS, it will be available to the general public, including foreign nations.

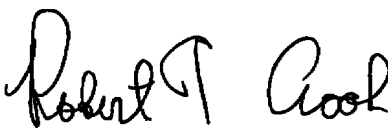
## APPROVAL STATEMENT

This report has been reviewed and approved.

  
JAMES D. MITCHELL  
Propulsion Technology  
Applied Technology Division  
Test Operations Directorate

Approved for publication:

FOR THE COMMANDER

  
ROBERT T. CROOK  
Asst Chief, Applied Technology Division  
Test Operations Directorate

REPORT DOCUMENTATION PAGE			Form Approved OMB No. 0704-0188
Public reporting burden for this collection of information is estimated to average 1 hour per response, including the time for reviewing instructions, searching existing data sources, gathering and maintaining the data needed, and completing and reviewing the collection of information. Send comments regarding this burden estimate or any other aspect of this collection of information, including suggestions for reducing the burden, to Washington Headquarters Services, Directorate for Information Operations and Reports, 1215 Jefferson Davis Highway, Suite 1204, Arlington, VA 22202-4302, and to the Office of Management and Budget, Paperwork Reduction Project (0704-0188), Washington, DC 20503.			
1. AGENCY USE ONLY (Leave blank)	2. REPORT DATE August 1995	3. REPORT TYPE AND DATES COVERED Final Report for October 1993 - April 1995	
4. TITLE AND SUBTITLE Application of a Modified Dynamic Compression System Model to a Low-Aspect-Ratio Fan: Effects of Inlet Distortion		5. FUNDING NUMBERS AF JN 0091 AF JN 2383	
6. AUTHOR(S) Shahrokhi, Kimball A., Sverdrup Technology, Inc., AEDC Group			
7. PERFORMING ORGANIZATION NAME(S) AND ADDRESS(ES) Arnold Engineering Development Center/DOP Air Force Materiel Command Arnold Air Force Base, TN 37389-5050		8. PERFORMING ORGANIZATION (REPORT NUMBER) AEDC-TR-95-16	
9. SPONSORING/MONITORING AGENCY NAME(S) AND ADDRESS(ES) Arnold Engineering Development Center/DOP Air Force Materiel Command Arnold Air Force Base, TN 37389-5050		10. SPONSORING/MONITORING AGENCY REPORT NUMBER	
11. SUPPLEMENTARY NOTES  Available in Defense Technical Information Center (DTIC).			
12A. DISTRIBUTION/AVAILABILITY STATEMENT  Approved for public release; distribution is unlimited.		12B. DISTRIBUTION CODE	
13. ABSTRACT (Maximum 200 words)  The objective of this research was to modify and calibrate a 1-D dynamic compression system model, DYNTTECC, to more accurately simulate compressor operation with steady, nonuniform inlet flow. The modifications were based upon parallel compressor theory, and modeled both circumferential and radial effects of distorted inlet flow. The modifications included circumferential and radial mass redistribution, dynamic blade response, and radial work redistribution. The circumferential mass redistribution allowed mass transport between adjacent circumferential segments within the compressor section, based on an orifice flow analogy. The radial mass redistribution allowed mass transport between adjacent radial segments, based on the radial momentum equation. The dynamic blade response modeled the compressor rotor blade's response to inlet circumferential pressure distortions. A dynamic lag ratio was used to damp the model's response to a flow disturbance. The simulation uses quasi-steady stage characteristics, and the lag ratio compensated for the finite response time of the rotor blade. The work redistribution utilized scale factors, allowing the stage characteristics to be defined as a function of radius. The model was calibrated to experimental data for clean and distorted inlet conditions for a two-stage, low-aspect-ratio fan. The distorted conditions were comprised of radial and circumferential total pressure distortion.			
14. SUBJECT TERMS inlet distortion, compressor, axial flow, pressure distortion, modeling, simulation, aerodynamic stability, fan		15. NUMBER OF PAGES 87	
		16. PRICE CODE	
17. SECURITY CLASSIFICATION OF REPORT UNCLASSIFIED	18. SECURITY CLASSIFICATION OF THIS PAGE UNCLASSIFIED	19. SECURITY CLASSIFICATION OF ABSTRACT UNCLASSIFIED	20. LIMITATION OF ABSTRACT SAME AS REPORT

## **PREFACE**

I would like to acknowledge Vanderbilt University, the United States Air Force, and Sverdrup Technology, Inc. for support provided at the Arnold Engineering Development Center, as well as the Compressor Research Facility, Wright-Patterson Air Force Base. I would also like to express my appreciation to the many individuals who have assisted and supported me throughout my studies. Dr. Milton W. Davis, Jr. is due a special thanks for introducing me to dynamic compressor modeling and for his guidance in my research effort. Thanks are also in order for G. Douglas Garrard for his guidance and insight that made the thesis effort bearable. A special thanks goes to Dr. John W. Williamson, Dr. Alvin M. Strauss, and Dr. Steven W. Peterson for their guidance and participation on my review committee. Thanks also go to Mr. Stephen A. Savelle for his help and guidance, and for reviewing this thesis. I would also like to acknowledge Mr. L. Brent Bates for his help in the review process. At the CRF, I would like to thank Mr. Steve Gorrell and Capt. Kevin Waters for their time and help. Additionally, I would like to thank Mrs. Vi Prosser for her invaluable help and guidance at Vanderbilt University. Thanks go to Major Hal Martin and Mr. Don Malloy for their help in getting me started at AEDC.

The research reported herein was performed by the AEDC; Air Force Materiel Command. Work and analysis for this research were done by personnel of Sverdrup Technology, Inc., AEDC Group, support contractor for the AEDC propulsion test facilities, under Air Force Job Numbers 0091 and 2383. The Air Force Project Manager was Mr. James D. Mitchell. The manuscript was submitted for publication on June 16, 1995.

## CONTENTS

	<u>Page</u>
PREFACE.....	1
1.0 INTRODUCTION .....	7
2.0 BACKGROUND .....	8
3.0 SIMULATION TECHNIQUE .....	12
3.1 DYNAmic Turbine Engine Compressor Code (DYNTECC) .....	12
3.2 Modified Compressor Model .....	13
4.0 MODEL COMPARISON.....	22
4.1 Experimental Data .....	22
4.2 Compressor Instability Criteria .....	23
4.3 Model Comparison -- Clean Inlet .....	23
4.4 Model Comparison -- Steady Distortion .....	24
5.0 SUMMARY .....	28
6.0 CONCLUSIONS .....	30
7.0 RECOMMENDATIONS FOR FUTURE WORK.....	31

## ILLUSTRATIONS

<u>Figure</u>	<u>Page</u>
1. Example of the Parallel Compressor Theory with Circumferential Segments and an Applied Inlet Distortion. ....	35
2. Results from Steenken's Research Showing the Predictions of the Modified Model and the Pure Parallel Model Versus Experimental Data. ....	35
3. Illustration of the Angular Displacement of the Circumferential Segments through the Rotor, Utilized in Mazzawy's Compressor Model .....	36
4. Example of the Distortion Index for a Circumferential Total Pressure Distortion Pattern	36
5. Schematic of the Physical Compression System and the Control Volume Concepts of the One-Dimensional Model .....	37
6. Example of Compressor Quasi-Steady Stage Characteristics .....	37
7. Illustration of the Circumferential Crossflow Model with the Orifice Flow Analogy ...	38
8. Classical Orifice Model Illustration .....	39
9. Plot of the Flow Coefficient for the Classical Orifice Model .....	39
10. Illustration of the Radial Crossflow Model .....	40
11. 180-deg Circumferential Distortion and its Effects on Flow Velocity Relative to the Rotor Blade .....	41

<b><u>Figure</u></b>	<b><u>Page</u></b>
12. Rotor Blade Coefficient of Lift as Blade Angle of Attack Varies . . . . .	42
13. Unsteady Lift Coefficient Magnitude Ratio . . . . .	42
14. Unsteady Blade Response to Circumferentially Nonuniform Flow Conditions . . . . .	43
15. Illustration of Work Redistribution Concept with Radial Variation of Pressure Ratios. . . . .	44
16. Compression System Model Geometry . . . . .	45
17. Pressure Rise as a Function of Percent Corrected Airflow . . . . .	46
18. Temperature Rise as a Function of Percent Corrected Airflow. . . . .	47
19. Clean Inlet Performance Model Prediction and Experimental Data (98.6-percent Rotor Speed). . . . .	48
20. Clean Inlet Performance Model Prediction and Experimental Data (85-percent Rotor Speed). . . . .	48
21. One/Revolution Total Pressure Distortion Screen. . . . .	49
22. Typical Inlet Total Pressure Pattern Produced by a One/Revolution Distortion Screen . . . . .	49
23. Total Pressure Distortion Pattern Produced by the One/Revolution Distortion Screen at 98.6-percent Corrected Rotor Speed . . . . .	50
24. Total Pressure Distortion Pattern Produced by the One/Revolution Distortion Screen at 85-percent Corrected Rotor Speed. . . . .	50
25. Compressor Performance Prediction for One/Revolution Circumferential Distortion Screen at 98.6-percent Corrected Rotor Speed. . . . .	51
26. Compressor Performance Prediction for One/Revolution Circumferential Distortion Screen at 85-percent Corrected Rotor Speed . . . . .	51
27. Distortion Attenuation for Circumferential Total Pressure Distortion at 98.6-percent Corrected Speed . . . . .	52
28. Distortion Attenuation for Circumferential Total Pressure Distortion at 85-percent Corrected Speed. . . . .	54
29. Typical Inlet Total Pressure Pattern Produced by a Hub-Radial Distortion Screen . . . . .	56
30. Total Pressure Distortion Pattern Produced by the Hub-Radial Distortion Screen at 98.6-percent Corrected Rotor Speed . . . . .	57
31. Total Pressure Distortion Pattern Produced by the Hub-Radial Distortion Screen at 85-percent Corrected Rotor Speed. . . . .	57
32. Compressor Performance Prediction for Hub-Radial Distortion Screen at 98.6-percent Corrected Rotor Speed . . . . .	58
33. Compressor Performance Prediction for Hub-Radial Distortion Screen at 85-percent Corrected Rotor Speed. . . . .	58

<b><u>Figure</u></b>	<b><u>Page</u></b>
34. Distortion Attenuation for Hub-Radial Total Pressure Distortion at 98.6-percent Corrected Speed .....	59
35. Distortion Attenuation for Hub-Radial Total Pressure Distortion at 85-percent Corrected Speed .....	61
36. Tip-Radial Total Pressure Distortion Screen .....	63
37. Typical Inlet Total Pressure Pattern Produced by a Tip-Radial Distortion Screen .....	63
38. Total Pressure Distortion Pattern Produced by the Tip-Radial Distortion Screen at 85-percent Corrected Rotor Speed .....	64
39. Compressor Performance Prediction for Tip-Radial Distortion Screen at 85-percent Corrected Rotor Speed .....	64
40. Distortion Attenuation for Tip-Radial Total Pressure Distortion at 85-percent Corrected Speed .....	65
41. Three-Dimensional Control Volume .....	67
42. Illustration for Stall Margin Calculations .....	67

## TABLES

<b><u>Table</u></b>	<b><u>Page</u></b>
1. Comparison of Model Predicted Instability Point Versus Experimental Data (Clean Inlet at 98.6-percent Speed) .....	68
2. Comparison of Model Predicted Instability Point Versus Experimental Data (Clean Inlet at 85-percent Speed) .....	68
3. Summary of Stall Margin Calculations for Model and Experimental Data at Both Speeds with Clean Inlet .....	68
4. Comparison of the Modified Model Predicted Instability Point Versus Experimental Data (One/Revolution Inlet Distortion Pattern at 98.6-percent Speed) .....	68
5. Comparison of the Modified Model Predicted Instability Point Versus Experimental Data (One/Revolution Inlet Distortion Pattern at 85-percent Speed) .....	69
6. Summary of Stall Calculations for Modified Model and Experimental Results (One/Revolution Inlet Distortion at 98.6-percent Speed) .....	69
7. Summary of Stall Calculations for Modified Model and Experimental Results (One/Revolution Inlet Distortion at 85-percent Speed) .....	69
8. Comparison of the Parallel Model Predicted Instability Point Versus Experimental Data (One/Revolution Inlet Distortion at 98.6-percent Speed) .....	70

<b><u>Table</u></b>	<b><u>Page</u></b>
9. Comparison of the Parallel Model Predicted Instability Point Versus Experimental Data (One/Revolution Inlet Distortion at 85-percent Speed) . . . . .	70
10. Work Redistribution Scale Factors for Both the Pressure and Temperature Characteristics for the 98.6-percent Speed . . . . .	70
11. Work Redistribution Scale Factors for Both the Pressure and Temperature Characteristics for the 85-percent Speed . . . . .	71
12. Comparison of the Modified Model Predicted Instability Point Versus Experimental Data (Hub-Radial Inlet Distortion at 98.6-percent Speed) . . . . .	71
13. Comparison of the Modified Model Predicted Instability Point Versus Experimental Data (Hub-Radial Inlet Distortion at 85-percent Speed) . . . . .	71
14. Summary of Stall Calculations for Modified Model and Experimental Results (Hub-Radial Inlet Distortion at 98.6-percent Speed). . . . .	72
15. Summary of Stall Calculations for Modified Model and Experimental Results (Hub-Radial Inlet Distortion at 85-percent Speed) . . . . .	72
16. Comparison of the Modified Model Predicted Instability Point Versus Experimental Data (Tip-Radial Inlet Distortion at 85-percent Speed). . . . .	72
17. Summary of Stall Calculations for Modified Model and Experimental Results (Tip-Radial Inlet Distortion at 85-percent Speed). . . . .	73

## **APPENDICES**

A. GOVERNING EQUATIONS . . . . .	75
B. STALL MARGIN CALCULATIONS. . . . .	81
NOMENCLATURE. . . . .	82



## 1.0 INTRODUCTION

Modern aircraft gas turbine engines are subject to continuing demands that are pushing engine performance capabilities to ever higher levels. As the operational envelope of gas turbine engines is stretched, stable operation of the engine and its components remains imperative. The engine must maintain stable operation as performance demands dictate that components operate at or near aerodynamic, thermodynamic, and structural limits. Stable operation must also be maintained through transient and dynamic events in a variety of adverse environments.

Nonuniform or distorted inlet airflow is one of the operational conditions that can affect compressor performance and operability. Pressure and temperature distortions are forms of inlet airflow nonuniformities that can occur for a variety of reasons. Pressure distortions, as a result of extreme combat maneuvers, and temperature distortions, as a result of exhaust gas ingestion from payload firing, are examples of nonuniform flow conditions. These inlet distortions can decrease compression system performance, and more importantly, decrease system stability limits. The compressor stability limit is reached when the airflow separates from the compressor rotor blades (i.e., stalled blades). The types of compression system instability are rotating stall and surge. Both types of instabilities lead to overall performance degradation and the potential for catastrophic system failure if they are allowed to persist.

To aid in the analysis of engine performance and operability, engineers rely on numerical simulations. Engine components can be mathematically modeled and combined with a numerical solution technique to provide a computer simulation of a physical system. Benefits of computer simulation use include the reduction in the amount of expensive ground testing of engines and their components, and investigation of events and conditions not easily tested in ground test facilities.

Compressor simulations take on several different forms, each with varying capabilities. Math models used in simulations range from one-dimensional to three-dimensional, with the capability of steady-state, transient (i.e., accurate model simulation of events less than 20 Hz), and/or dynamic (i.e., accurate model simulation of events greater than 20 Hz) operation. Increasing the capabilities and degrees of complexity results in an increase in required computational power. The varying attributes and capabilities of different models make it important to select an appropriate simulation that is capable of providing the necessary information at a minimal computational cost.

The objective of the current research is to improve the predictive capabilities of a one-dimensional, dynamic compression system model when investigating inlet flow distortion. The current methodology uses parallel compressor theory when examining cases with nonuniform inlet flows. In parallel compressor theory, the compression system is divided into circumferential segments or "tubes" that extend axially through the compressor (Fig. 1). All segments are treated

as individual compressors without interaction between segments. The segments share the same stage performance curves and a common exit static pressure boundary condition. The inlet boundary conditions are specified differently for each segment. In terms of compressor instability or stall, the compressor is considered stalled if one or more segments become unstable (Ref. 1).

Parallel compressor theory is generally valid if the segment arc is greater than 60 deg, also known as the critical angle (Ref. 1). Secondary flow mechanisms become more significant for segment arcs of less than the critical angle. The parallel compressor theory's predictive capabilities deteriorate when segment arcs drop below the critical angle (Ref. 1).

Modifications to the one-dimensional compression system model are based on the parallel compressor theory. The modified model allows interactions between segments to improve the model's predictive capabilities with complex inlet distortion patterns (i.e., segment angles below the critical angle). The model modifications include algebraic expressions that model the three-dimensional flow effects caused by the inlet flow distortion. The modified model is calibrated to experimental data from a two-stage, low-aspect-ratio fan under several inlet flow disturbances.

The following section briefly addresses previous work in the area of compression system modeling and prediction of system performance and operability with nonuniform inlet flow. A discussion of a selected one-dimensional compression system (Ref. 2) model is given. Modifications to the compression system model are discussed, along with their impact on the model's predictive capabilities with nonuniform inlet flow. Model results are compared to experimental values for several distorted inlet flows. A summary of conclusions is presented based on the analysis of the improved model predictions, and recommendations for further work are suggested.

## 2.0 BACKGROUND

One of the earliest modeling efforts to address inlet distortion and its effects on compression system operability was by Korn (Ref. 3). The modeling method that Korn used was based on the classical parallel compressor theory, with modifications to account for more realistic rotor response to dynamic events. He points out that while the classic parallel compressor theory produces relatively good results in some instances, they are often conservative in their prediction of compressor instability.

Korn discussed the response of the compressor rotor to dynamic events, noting that the lift response of the blades on a rotor cannot change instantaneously to a dynamic event. This damped response can have an important role when the compressor is operating near the limit of stable compressor operation, or stability limit. Korn argued that when the compressor is near the limit, it

is possible for the flow incident to the blade to be beyond the steady-state stability limit criteria without the blade actually stalling. The concept of rotor stall delay was introduced, along with an effective frequency of nonuniform flow on the compressor rotor. This effective frequency is similar in concept to the reduced frequency introduced by Goethert and Reddy (Ref. 4), which will be discussed later in this section.

Steenken presented two extensions to a quasi-one-dimensional, time-dependent, blade row model (Ref. 5). One extension involved radial mass redistribution, while the other extension involved circumferential mass redistribution. Both of these mass redistributions allow mass transfer between the multiple, parallel segments that are used to define the compression system.

As in the basic parallel compressor theory, Steenken's models utilized the axial mass, momentum, and energy equations. The radial and circumferential redistribution models also solved their respective momentum equations. The model using radial mass redistribution allowed for redistribution upstream and downstream of the compressor. The circumferential model also allowed mass redistribution upstream and downstream of the compressor, as well as within the compressor itself if the blade-free volumes are significantly large.

Both the circumferential redistribution model and the classical parallel compressor theory model were used to examine a 180-deg circumferential inlet total pressure distortion placed upon a single-stage fan. The pure parallel model utilized two circumferential segments to define the inlet total pressure conditions, while the redistribution model used six circumferential segments. The redistribution model also was examined in two configurations: one with a uniform exit static pressure boundary condition or abbreviated model, and the other with a nonuniform exit static pressure boundary condition. The nonuniform exit condition was used to describe more accurately the actual exit boundary conditions of the compression system being examined.

Using the modified model and comparing to test data, the predictions of overall compressor pressure rise as a function of percent corrected airflow were significantly better than the pure parallel (See Fig. 2). This example is based on a single-stage fan with a 180-deg circumferential distortion pattern. One interesting aspect of the predictive capabilities of the abbreviated model is that the results proved to be closer to the experimental test data than the full model (i.e., non-uniform exit boundary condition). The author failed to reach any conclusions as to the cause of the apparent discrepancy, but cites other research that shows that different results would be obtained depending on the discharge conditions of the compressor (e.g., exit to a nozzle, constant area duct, etc.). A similar blade row model is also applied to a J85 turbine engine by Tesch and Steenken (Ref. 6). When using distribution models, the authors saw significant improvements over the classical parallel compressor model in the prediction of compressor instability.

A multiple segment model also based on the parallel compressor theory was developed by Mazzawy (Ref. 7). This model, however, took a more radical departure from the classic parallel compressor theory than the previous two models discussed. Mazzawy presents two forms of the model that avoid assumptions made in the classic parallel compressor theory. The parallel compressor theory bases the performance of any individual sector, even with distorted flow, on the overall, steady-state, clean inlet compressor characteristics. Mazzawy stated that the distorted overall compressor performance in any circumferential sector can be different from the undistorted compressor performance with the same boundary conditions. This difference from the clean inlet performance is attributable to unsteady flow effects and distortion-induced compressor stage matching differences.

The parallel compressor theory also has the assumption of a circumferentially uniform exit static pressure. Mazzawy contended that this is often an invalid assumption since a nonuniform exit static pressure can be generated by a downstream diffuser or by another compressor in a multispool configuration.

The models Mazzawy developed were in two forms, one with blade-row characteristics and the other with overall compressor characteristics. The first model that Mazzawy presented is one with multiple parallel segments and individual blade-row performance characteristics. The model accounted for the two-dimensionality of a circumferentially distorted flow field through a unique method. In the classic parallel compressor theory, it is assumed that each segment has the same circumferential alignment at the exit as it does at the entrance. In the Mazzawy model, the circumferential segments move in the circumferential direction as they pass through the compressor. This translation was based on the fact that the mean flow angles are seldom axial through the rotor, stator, and associated gaps or blade-free regions. The model provided additional angular displacement to the segments based on the rotation of the rotor, as is shown in Fig. 3. The model also allowed for circumferential mass redistribution upstream of the compressor.

The second model presented by Mazzawy was similar to the first, except for the use of overall compressor performance characteristics instead of the blade-row characteristics. This model also provided approximate correlations for unsteady flow effects, circumferential particle swirl, and upstream flow redistribution.

Both models provided a significant improvement over the classic parallel compressor theory in the prediction of compressor operability, as well as an improved prediction capability of distortion attenuation through the compressor. Distortion sensitivity, or stall margin loss predictions were also improved. However, Mazzawy states that the distortion sensitivity or stall margin loss predictions were subject to extrapolations of quasi-steady compressor performance characteristics below the clean inlet stall airflow. These extrapolations mean that the model was forced to extrapolate information into the post-stall regime where no characteristics were provided.

Mazzawy and Banks also applied the multiple segment, blade row model to the TF30-P-3 turbofan engine in an examination of inlet circumferentially distorted flow (Refs. 8–9). Model predictions and experimental results were compared for model calibration, with predicted results within  $\pm 5$  percent of experimental. Application of the model included analysis of distortion attenuation and compressor stall sensitivity. Overall stall prediction was based upon parallel compressor theory and proved to be too conservative in stability limit prediction.

Longley and Greitzer (Ref. 1) examined steady circumferential inlet flow distortion effects with a compressor model that was based on the parallel compressor theory. The authors mainly focused on compressor stability and stall prediction with respect to the distorted inlet flows.

The model used by Longley and Greitzer was based on the classical parallel compressor theory with overall compressor characteristics and multiple segments, each operating at a local flow rate. Instability was said to occur when one of the parallel segments reached an instability limit. When the authors examined distorted inlet flow, they found the model was extended beyond the basic parallel compressor theory with the modification of the compressor stall prediction criteria. This modification to the stall prediction was through the use of a distortion index. The index related the severity of the distortion in terms of the size of the distortion total pressure region, as well as a critical region size. The distorted region was discussed in terms of a spoiled sector with an associated angle, and the critical region size was discussed in terms of a critical sector angle. The distortion index,  $DC(\theta_{crit})$ , was defined as

$$DC(\theta_{crit}) = \frac{P_{t|360^\circ} - P_{t|worst\theta_{crit}}}{\frac{1}{2}\rho U^2} \quad (1)(\text{Ref. 1})$$

An example for a critical sector angle,  $(\theta_{crit})$ , of 60 deg is illustrated in Fig. 4.

When examining a spoiled sector of relatively small size (i.e., smaller than the critical sector angle), the stall margin loss is proportional to the distortion index. With the critical sector angle concept, the compressor instability is said to occur when a weighted average of the high and low flow sectors reaches the uniform flow stability boundary, or stall line. This concept also implies that a sufficiently "narrow" spoiled sector can operate beyond the clean inlet stability line if there is a sufficiently large proportion of the annulus that is operating below the stability line.

Kimzey's (Ref. 10) work was also based on the classical parallel compressor theory. Kimzey sought to refine the pure parallel compressor theory to better compensate for the three-dimensional aspects of complex inlet distortion patterns. Refinements to the parallel compressor theory included

both circumferential and radial mass redistributions, radial work redistribution, and a dynamic blade lagging function. These refinements were based on algebraic expressions instead of solving the full set of three-dimensional equations. The enhanced model was used to investigate several compression systems with pressure and temperature inlet distortions. The foundation of the current research is based on the enhanced one-dimensional model by Kimzey.

The work initiated by Kimzey was pursued by Hale and Davis (Ref. 2), and culminated in a compression system simulation known as DYNTTECC. This simulation is a dynamic, one-dimensional, stage-by-stage model and simulation that solves the conservation of mass, momentum, and energy equations using a finite-difference method. The simulation includes turbomachinery source terms that were derived from quasi-steady stage characteristics. DYNTTECC uses pure parallel compressor theory when investigating inlet distortions.

Hale and Davis successfully used the DYNTTECC simulation to model a ten-stage axial-flow compressor (Ref. 2). Investigations included pre- and post-stall operations, single- and dual-spool configurations, and pressure and temperature inlet distortions. DYNTTECC successfully predicted stability limits for the inlet distortion patterns investigated, including investigations of 180-deg total pressure distortion patterns for the 10-stage compressor. DYNTTECC was also used to investigate a combination of pressure and temperature distortions and hot gas ingestion (Ref. 11).

The DYNTTECC simulation is the baseline code for the current research, with modifications that will enhance the predictive capabilities of DYNTTECC when investigating inlet pressure distortions. The goal of the research is to implement technology developed by Kimzey into a modern dynamic compression system simulation, DYNTTECC.

### **3.0 SIMULATION TECHNIQUE**

#### **3.1 DYNAMIC TURBINE ENGINE COMPRESSOR CODE (DYNTTECC)**

The DYNTTECC model calculates the performance and operability of stage-by-stage, one-dimensional compression systems. The axial mass, momentum, and energy equations are solved simultaneously using a finite-difference technique. Turbomachinery source terms such as mass bleeds, blade forces, and shaft work that are determined from pressure and temperature stage characteristics are included. Hale and Davis provide a detailed discussion of the theory and capabilities of DYNTTECC (Ref. 2).

The overall control volume used in DYNTTECC is divided into elemental control volumes as shown in Fig. 5. A typical compressor is divided into elemental control volumes by stages using a rotor-stator or stator-rotor combination for which stage characteristics have been determined.

Ducting sections of the system are divided into control volumes to ensure appropriate frequency response. The three governing equations of mass, momentum, and energy are applied to an individual control volume. These equations can be expressed as follows:

$$\frac{\partial}{\partial t}(\bar{Q}A) + \frac{\partial}{\partial x}(\bar{F}A) = \bar{S} \quad (2)$$

where

$$\bar{Q} = \begin{Bmatrix} \rho \\ \rho U \\ e + \frac{U^2}{2} \end{Bmatrix}; \bar{F} = \begin{Bmatrix} \rho U \\ \rho U^2 + P \\ \rho U \left( e + \frac{P}{\rho} + \frac{U^2}{2} \right) \end{Bmatrix}; \bar{S} = \begin{Bmatrix} -W_{Bx} \\ F_x \\ Q_x + S_x - H_{Bx} \end{Bmatrix}$$

The axial-force distribution,  $F_x$ , represents the compressor blading forces and the casing forces produced by the compressor walls. The heat-transfer rate and compressor shaft work are represented by the  $Q_x$  and  $S_x$  terms, respectively. The  $W_{Bx}$  term represents the mass flow across the system boundaries other than the inlet or exit, typically an interstage bleed.

Turbomachinery source terms for the momentum and energy equations are calculated using quasi-steady stage characteristics that provide pressure and temperature variations as a function of air-flow, as shown in Fig. 6. The example stage characteristics in Fig. 6 show three distinct regions of compressor operation: pre-stall, rotating stall, and reverse flow. The rotating stall and reverse flow regions are post-stall operating regimes that are beyond the scope of this research. The investigation of the model modifications with distorted inlet flow is restricted to pre-stall operation.

### 3.2 MODIFIED COMPRESSOR MODEL

The current research extends the DYNTECC model beyond the basic parallel compressor theory. The goal of the modified model is to provide a more accurate predictive tool for compressor performance and operability with inlet distortions. The modified one-dimensional equations are presented with additional terms to compensate for additional flow effects. The model modifications include circumferential and radial mass redistribution, dynamic blade response, and radial work redistribution, all of which will be discussed in the following sections.

### 3.2.1 Modified One-Dimensional Equations

The modified, one-dimensional equations are based on derivations made by Kimzey (Ref. 10) and are presented in Appendix A. The modified equations model the three-dimensional effects of a distorted flow. In order to model the effects, approximations and basic assumptions are necessary to allow the one-dimensional equations to accurately account for the additional flow effects.

In order to understand the additional effects' impact on the one-dimensional equations, we begin with the continuity equation. To allow additional mass transport in the radial and circumferential directions, the continuity equation is written in the following form

$$\frac{\partial(\rho A)}{\partial t} + \frac{\partial(\rho UA)}{\partial x} = -W_{Bx} + (-WR_{net} + WC_{net}) \quad (3)$$

The terms  $WR_{net}$  and  $WC_{net}$  are the net mass flows entering the control volume in the radial and circumferential directions, respectively. The two terms are defined in the current research as the radial and circumferential mass redistribution, or crossflow, terms. Since these terms are determined from models to be discussed, they are treated like source terms and have been lumped in with the bleed flow source term,  $W_{Bx}$ . The origins of the approximations for these terms are outlined in the following sections.

An assumption is made of small radial and circumferential velocities,  $v$  and  $w$ , as compared to the axial velocity,  $U$ . Thus, the momentum across the radial and circumferential boundaries is deemed negligible compared to the axial momentum (Ref. 10). The axial equation for momentum is

$$\frac{\partial(\rho UA)}{\partial t} + \frac{\partial(\rho U^2 + P)A}{\partial x} = F_x \quad (4)$$

The contribution of the pressure integrated over the projected areas of the radially oriented surfaces is combined with the force term  $F_x$  (Ref. 10). This combined term is necessary because of the difficulty in isolating from experimental data the blading force term (Ref. 12). The source terms are calculated by the model from compressor stage characteristics provided by the user.

In the energy equation, the assumption of small  $v^2$  and  $w^2$  terms as compared to the  $U^2$  term results in no change in the energy equation.

$$\frac{\partial\left(e + \frac{U^2}{2}\right)A}{\partial t} + \frac{\partial\left(\rho U\left(e + \frac{p}{\rho} + \frac{U^2}{2}\right)A\right)}{\partial x} = Q_x + S_x - H_{Bx} \quad (5)$$



The terms neglected were determined by Kimzey (Ref. 10) to be second-order terms through non-dimensionalization and order of magnitude analysis. In addition, the enthalpy terms are neglected from the overall energy equation that is solved. For a total pressure distortion, the temperatures in adjacent control volumes in the same axial plane are assumed to be approximately equal. Therefore, there will be no net change in enthalpy due to the mass transported between control volumes. The impact of the crossflow terms on the energy equation is said to be negligible because of the relatively small radial and circumferential velocities and the negligible enthalpy transported between control volumes in the same axial plane.

### 3.2.2 Circumferential Mass Redistribution

A full three-dimensional compression system model implies implementation of the circumferential momentum equation. A simpler approach that utilizes a one-dimensional model and some simple analogies has been applied to reduce the complexity of the model and decrease the simulation execution time. The approach taken models the effects of the circumferential momentum equation.

Inlet pressure distortions with circumferential nonuniformities can generate mass flow in the circumferential direction. The static pressure difference between two segments can drive a flow in the circumferential direction. This flow would occur in the gap between the compressor rotor and stator (See Fig. 7). The circumferential mass flow within the rotor-stator gap can be approximated using a simple orifice flow analogy, a concept developed by Kimzey (Ref. 10). In the analogy, the high and low static pressure regions are modeled as pressure reservoirs separated by an orifice, representing the rotor-stator gap. Thus, the flow can be approximated utilizing a simple algebraic expression based on a classic orifice flow, as illustrated in Fig. 8.

The model is based upon the basic assumption of incompressible flow through the orifice. From Ref. 13, orifice flows with small pressure drops can be treated as incompressible flows. Using the continuity equation and Bernoulli's equation for steady flow and assuming no work, heat transfers or change in elevation provides the framework for the model as mathematically described in the following equation:

$$p_1 - p_2 = \frac{\rho}{2} (V_2^2 - V_1^2) = \frac{\rho V_2^2}{2} \left[ 1 - \left( \frac{V_1}{V_2} \right)^2 \right] \quad (6)$$

and

$$\left( \frac{V_1}{V_2} \right)^2 = \left( \frac{A_1}{A_2} \right)^2 \quad (7)$$

Substituting, one can solve for the ideal exit velocity.

$$V_2 = \sqrt{\frac{2(p_1 - p_2)}{\rho [1 - (A_2/A_1)^2]}} \quad (8) \text{ (Ref. 13)}$$

Using the orifice area and constant density, the above velocity can be used to solve for the theoretical mass flow rate.

$$W_{theoretical} = \frac{A_2}{\sqrt{1 - (A_2/A_1)^2}} \sqrt{2\rho (p_1 - p_2)} \quad (9) \text{ (Ref. 13)}$$

Using empirical relationships, an expression for the actual mass flow rate through the orifice can be attained based on the ideal expression.

Because of the presence of vena contracta, the effective diameter  $D_2$  is unknown, thus requiring that the diameter of the orifice be used. A discharge coefficient will correct for the discrepancy, as well as any frictional loss. The orifice discharge coefficient,  $C$ , is a function of the ratio of actual mass flow rate versus the theoretical mass flow rate.

$$C = \frac{\text{actual mass flow rate}}{\text{theoretical mass flow rate}} \quad (10)$$

A parameter  $\beta$  is also used which is a ratio of orifice throat diameter to inlet diameter.

$$\beta = \frac{D_t}{D_1} \quad (11)$$

One must note that in the case of a circumferential crossflow in an axial compressor, the passage is actually a rectangle. Therefore, the diameters presented above should be expressed as hydraulic diameters.

The equation for the actual mass flow rate can now be expressed in terms of the theoretical mass flow rate and the two new parameters.

$$W_{actual} = \frac{CA_t}{\sqrt{1 - \beta^4}} \sqrt{2\rho (p_1 - p_2)} \quad (12) \text{ (Ref. 13)}$$

The discharge coefficient and the geometric parameter are typically combined into a single flow coefficient,  $K$ , for the orifice.

$$K = \frac{C}{\sqrt{1 - \beta^4}} \quad (13) \text{ (Ref. 13)}$$

The final equation for the actual mass flow rate is now in terms of the new flow coefficient and a pressure difference.

$$W_{actual} = KA_t \sqrt{2\rho (p_1 - p_2)} \quad (14) \text{ (Ref. 13)}$$

The orifice flow coefficient,  $K$ , is in our case referred to as a circumferential crossflow coefficient,  $K_c^*$ .

$$WC_{net} = K_c^* A_t \sqrt{2\rho (p_1 - p_2)} \quad (15)$$

Illustrated in Fig. 9 are the values of the orifice flow coefficient versus flow Reynolds number taken from Ref. 13. For an orifice with pronounced vena contracta and a high Reynolds number, the curves converge at a flow coefficient of approximately 0.6.

### 3.2.3 Radial Mass Redistribution

Looking axially through the compressor, secondary radial mass flow can occur in the passages between the compressor blades. The mass flux in the radial direction, referred to as the radial mass redistribution or crossflow, is similar in concept to the circumferential crossflow. Both circumferential and radial mass fluxes across segment boundaries are due to differences in static pressure that drive the secondary flow (See Fig. 10) (Ref. 10). As with the circumferential crossflow, the model for the radial crossflow is a simple algebraic expression used to approximate the mass flux. However, the expression is derived from the radial momentum equation rather than through the use of an analogy.

The radial momentum equation (See Appendix A) is simplified by neglecting the time-dependent term as well as the flux terms across all but the radial facing control volume boundaries (Ref. 10). Evaluating for radial segments with a static pressure gradient (Fig. 10), an equation for the net mass flux in the radial direction is

$$WR_{net} = K_R \sqrt{\rho_{low} (PS_{high} - PS_{low})} * A^2 + FR * A \quad (16)$$

The force term,  $FR$ , includes centrifugal as well as viscous force terms.

$$FR = F_{viscous} + \rho (\text{volume}) \omega^2 r \quad (17) \text{ (Ref. 10)}$$

The mass flux term is a net mass flux due to distortion. When no distortion is present, the flux term goes to zero. Therefore, the  $FR$  term must be adjusted such that the  $WR_{net}$  term is approximately zero when no distortion is present.

For the current research, a simpler equation for the radial mass redistribution was sought. This simpler approach sought to combine the two calibration coefficients,  $FR$  and  $K_R$ , into a single coefficient. The purpose of the simplified approach is to attempt to gain an additional measure of insight into the nature of the coefficient with respect to the phenomena being modeled.

This simpler approach is a derivation similar to the derivation necessary for the orifice flow model. Based on the Bernoulli equation, the theoretical mass flow rate driven by a radial static pressure gradient takes on the form of

$$WR_{net, \text{theoretical}} = \frac{A_{low}}{\sqrt{1 - (A_{low}/A_{high})^2}} \sqrt{2\rho (PS_{high} - PS_{low})} \quad (18)$$

This equation assumes steady, incompressible, frictionless flow. In order to determine the actual mass flow rate in the radial direction, a term is added to account for additional flow effects, such as viscous and centrifugal forces.

$$WR_{net, \text{actual}} = (1 + \hat{k}) WR_{net, \text{theoretical}} \quad (19)$$

Setting the radial crossflow coefficient,  $K_R^*$ , equal to the multiplier in the above equation, an equation for the net mass flux in the radial direction is attained.

$$WR_{net, \text{actual}} = K_R^* \frac{A_{low}}{\sqrt{1 - (A_{low}/A_{high})^2}} \sqrt{2\rho (PS_{high} - PS_{low})} \quad (20)$$

### 3.2.4 Dynamic Blade Response

A circumferential pressure distortion on the inlet of a compressor with a low pressure spanning 180 deg is illustrated in Fig. 11. This pressure distortion is non-varying with respect to time and is therefore referred to as a steady distortion. However, from the perspective of an individual blade on the moving rotor encountering the steady distortion, the distortion appears to

vary with time. The rotor blade effectively experiences a change in its angle of attack,  $\alpha$ , due to the change in the relative velocity incident upon the blade leading edge, often referred to as unsteady cascade effects.

The two components of the relative velocity are the axial and the tangential velocities (See Fig. 11).

$$V_{rel} = U + V_\theta \quad (21)$$

The tangential velocity,  $V_\theta$ , also has two components consisting of the tangential velocity of the blade due to rotor speed, as well as the swirl velocity,  $V_{swirl}$ , produced by the circumferential pressure distortion.

$$V_\theta = \omega r + V_{swirl} \quad (22)$$

The presence and direction of the swirl velocity generated by the distortion produces the change in the relative flow velocity and, subsequently, the angle of attack,  $\alpha$ . The velocity diagrams illustrated in Fig. 11 show the change in the rotor blade angle of attack. The 180-deg circumferential distortion produces swirl velocities in opposite directions at the 90- and 270-deg locations. For the 0- and 180-deg locations, the swirl velocities are negligible. The velocity diagrams are depicted for the 0-, 90-, 180-, and 270-deg locations and show the effect of the presence and direction of the swirl velocity.

A detailed analysis of unsteady cascade effects can be found in Goethert and Reddy (Ref. 4). Goethert and Reddy state that there are significant differences in a stationary cascade with an oscillating flow, and an oscillating cascade with a stationary flow. In the case of a stationary cascade with an oscillating flow, the cascade will see the frequency,  $f$ , of the oscillating flow. In the case of a stationary flow and an oscillating cascade, the cascade sees an effective frequency dependent upon several terms, including the relative velocity,  $V_{rel}$ .

Goethert and Reddy used the concept of reduced frequency,  $k$ , which can be described as the ratio of the flow passage time to the disturbance stay time. The passage time is the ratio of the blade chord length to the relative velocity.

$$\Delta t_{passage} = \frac{C}{V_{rel}} \quad (23) \text{ (Ref. 4)}$$

The disturbance time is inversely proportional to the frequency of the oscillating motion of the cascade.

$$\Delta t_{disturbance} = \frac{1}{2f} \quad (24) \text{ (Ref. 4)}$$

The ratio of the passage time to the disturbance time is the reduced frequency.

$$\frac{k}{\pi} = \frac{\Delta t_{\text{passage}}}{\Delta t_{\text{disturbance}}} = \frac{2fC}{V_{\text{rel}}} = \frac{2NC}{60V_{\text{rel}}} \quad (25) \text{ (Ref. 4)}$$

There are limitations in the ability of the blade row to respond to rapid changes in the angle of attack. For rapid changes in the angle of attack, the blade requires a finite amount of time to adjust to the new flow conditions. Thus, the rate of change of the angle of attack with respect to time,  $\dot{\alpha}$ , can have a significant impact on the blade's response. Goethert and Reddy (Ref. 4) state that the blade dynamic response should be expected to be "sluggish" because of the boundary-layer effects not included in their inviscid analysis (Ref. 10). Kimzey states that this effect is particularly true near the stall point. Illustrated in Fig. 12 is a phenomenon of transient blade operation at high angles of attack without stalling.

Kimzey (Ref. 10) used the concept of reduced frequency to determine the response of a blade row to the oscillating flow conditions. Illustrated in Fig. 13 is a first-order approximation of the blade response in terms of the coefficient of lift, based on the analysis of Goethert and Reddy (Ref. 4).

$$\frac{dC_l}{dt} + \frac{C_l}{\tau} = \frac{C_{l,ss}}{\tau} \quad (26) \text{ (Ref. 10)}$$

The blade time constant,  $\tau$ , is a function of chord length and reduced frequency,

$$\tau = \frac{\epsilon C}{V_{\text{rel}}} \quad (27) \text{ (Ref. 10)}$$

where  $\epsilon$  is dependent upon cascade geometry (e.g., stagger angle, aspect ratio) (Ref. 10). The approximation for the first-order solution is

$$\frac{|C_l|_{\text{max}}}{|C_l|_{ss}} = \sqrt{\frac{1}{1 + (\epsilon k)^2}} \quad (28) \text{ (Ref. 10)}$$

Kimzey showed that the dynamic response of the coefficient of lift is the same as the dynamic response of the stage loading parameter,  $\psi$ .

$$\frac{|\psi|_{\text{max}}}{|\psi|_{ss}} = \frac{|C_l|_{\text{max}}}{|C_l|_{ss}} = \text{DLR} \quad (29) \text{ (Ref. 10)}$$

The dynamic lag algorithm developed by Kimzey introduces a dynamic lag ratio into the stage characteristics, in the form of

$$\Psi_{present\ c.v.} = DLR \Psi_{present.ss\ c.v.} + (1 - DLR) \Psi_{previous\ c.v.} \quad (30)$$

where

$$DLR = \sqrt{\frac{1}{1 + (\epsilon k)^2}} \quad (31) \text{ (Ref. 10)}$$

The effect of the lag algorithm on the compressor response to a circumferential inlet distortion is shown in Fig. 14.

The model uses quasi-steady stage characteristics to determine the blade's response to given operating conditions. The example shown in Fig. 14 has an inlet pressure distortion on a compressor divided into eight segments. Solely based on the quasi-steady characteristics, a segment with a sufficiently low inlet pressure and corresponding low flow rate may enter into an unstable operating region.

Based on Goethert and Reddy (Ref. 4), Kimzey (Ref. 10) argued that a segment with a relatively small angle can fall below a critical flow point and still be considered to be in stable operation. This argument is based on the finite response time of a compressor rotor blade to an instantaneous change in angle of attack. Essentially, the segment can enter and leave a "stalled" region and remain stable if the associated stay time is short enough.

To quantify the above argument, a dynamic lag ratio is used to model the blade's response to a change in angle of attack. The dynamic lag ratio, DLR, damps the model's response to a flow disturbance. The DLR compensates for the dynamic response of the rotor blade (See Fig. 14). Effectively, the results represent a set of dynamic characteristics for the compressor stages.

### 3.2.5 RADIAL WORK REDISTRIBUTION

Axial-flow compressors do not have uniform blade loading in the radial direction (Ref. 10). This radially nonuniform blade loading is addressed in the modified model through a form of radial work redistribution. The redistribution model seeks to radially distribute the work done across the blade to more accurately reflect experimental observations.

Kimzey (Ref. 10) outlined a radial work redistribution model that accounted for the pressure and temperature rises across a stage as a function of compressor radius,  $\psi = f(r)$ . The relationships

were based on the experimental results of pressure and temperature distributions across the individual compressor stages. The current work redistribution model is a simpler form of the model used by Kimzey. The model uses scale factors to adjust the steady-state stage characteristics to represent experimental observations more accurately. Applying simple scale factors for each of the radial segments per individual stage proved to be suitable for the simple, 5-radial segment geometry used.

In terms of clean inlet compressor performance, the method described above should have no impact on overall performance prediction. The model still utilizes stage characteristics that are based on overall compressor stage performance. The work redistribution methodology allows the stage characteristic to be calibrated at each radial segment for each stage of the compressor. Illustrated in Fig. 15 is an example of the work redistribution methodology.

#### **4.0 MODEL COMPARISON**

The current research involved comparison of several model cases against experimental data for a variety of compressor inlet conditions. The model was initially compared to the experimental clean inlet performance of the compressor, then the model was subsequently compared to experimental compressor performance for three different inlet distortion patterns. One pattern was purely circumferential, while the other two were purely radial patterns.

##### **4.1 EXPERIMENTAL DATA**

The physical system used to collect the data for the comparison of the model is a two-stage, low-aspect-ratio fan similar to the compression system examined by Gorrell and Davis (Ref. 14). The information is courtesy of the Compressor Research Facility at Wright-Patterson Air Force Base. The model representation of the compression system geometry is illustrated in Fig. 16.

The experimental data consisted of information for clean and distorted inlet compressor operation for two corrected rotor speeds, 98.6 and 85 percent relative to the design speed. The data included stage characteristic information in the form of pressure and temperature coefficients as a function of a flow coefficient. The normalized, experimentally determined stage characteristics are shown in Figs. 17a-b for the pressure coefficient and Figs. 18a-b for the temperature coefficient.

Typical measurements included ambient pressure and temperature that were taken upstream of the inlet bellmouth. Both static and total pressure measurements and total temperature measurements were taken within the inlet ducting upstream of the compressor section. Measurements were made in several locations in and about the compressor section itself to allow the characterization of compressor operation. Locations included the inlet guide vanes, the first-



stage exit stators, the second-stage exit stators, and a discharge rake downstream of the final exit stators. Total pressure distortion patterns produced by distortion screens were characterized by pressure probe rakes. These rakes provided readings for total pressure as a function of radial and circumferential location, in order to characterize the distortion produced by the screen.

## **4.2 COMPRESSOR INSTABILITY CRITERIA**

The experimentally determined stall point for a given speed was determined through a standard procedure. For a given speed, the compressor was forced into unstable operation through the closing of the compressor test rig throttle. The throttle was then opened enough to bring the compressor out of stall, and a data point was taken. This data point represents the experimental stability limit, which is in reality the last stable operating point.

For the compressor model, the stability limit for an individual stage was defined as the point at which the tangent to the pressure characteristic has a zero slope. For non-distorted inlet flow, the model stability limit was reached when both stages reached their stability limits. For parallel compressor theory, the simulation was said to have reached the stability limit, or have stalled, when one or more circumferential segments of the parallel representation had reached the defined stability limit.

For the modified model, this criterion was adjusted to allow more realistic simulation of the compressor in question. The criteria define a stage as stalled if 25 percent or more of its segments were stalled. For overall compressor stall, a criterion of 25 percent of the segments for both stages must be stalled.

## **4.3 MODEL COMPARISON -- CLEAN INLET**

Comparisons of clean inlet performance and operability model predictions against experimental data were made for the two corrected rotor speeds, 98.6 and 85 percent. The model began execution at a nominal operating point far from stall, and was allowed to come to a steady-state condition. Once the model reached steady-state, the exit static pressure was linearly increased at a rate of 100 psia/sec (i.e., representative of a combustor fuel pulse) until system instability was indicated.

Model prediction of compressor performance and operability was excellent for both speeds, as shown in Figs. 19 and 20. For the 98.6-percent speed, the model performance prediction was within 1 percent and 0.2 percent for the corrected airflow and pressure ratio, respectively, across the whole speedline. Model performance predictions for the 85-percent speed were within 0.4 percent and 0.65 percent for compressor airflow and pressure ratio, respectively.

Prediction of the compressor stall point for both speeds was also excellent. As is presented in Tables 1 and 2, the predicted airflow and pressure ratio at instability were within 1 percent and 0.16 percent for both the 98.6- and 85-percent speeds, respectively. Table 3 summarizes the stall margin calculations for the 98.6- and 85-percent speeds, based on the SAE's Aerospace Recommended Practice (ARP) 1420 standard (Ref. 15). (See Appendix B).

#### **4.4 MODEL COMPARISON — STEADY DISTORTION**

Three inlet distortion cases are used for comparison of the modified compressor model. The cases include data collected using screens producing both pure circumferential and pure radial total pressure distortions. The circumferential distortion was produced by a once-per-revolution (one/revolution) screen. The radial distortions were produced by both a tip-radial and a hub-radial screen. The following sections detail the results of the investigations.

##### **4.4.1 One/Revolution Circumferential Distortion**

The first distortion case to be examined is the pure circumferential inlet distortion. A typical circumferential pressure distortion screen is illustrated in Fig. 21. This screen is referred to as a one/revolution distortion screen due to the single low-pressure area per rotor revolution. A total pressure distortion pattern produced by the screen is shown in Fig. 22. Because of the screen geometry, the compressor inlet was divided into eight circumferential segments to accurately define the inlet distortion pattern.

Because a pure circumferential pattern was produced, only those modifications to the model that have a significant impact on the model predictions were activated (i.e., circumferential mass redistribution and the dynamic blade response). This modified model is compared to the experimental data, as well as the parallel compressor theory only.

Both the 98.6- and 85-percent corrected speeds are examined. The total pressure distortion patterns for the two speeds are illustrated in Figs. 23 and 24. The model began execution at a nominal operating point far from stall with a clean inlet to allow the model to attain a steady-state condition. After reaching steady-state, the distortion pattern was linearly ramped to its final distortion magnitude over a 0.04-sec time period. Once the steady-state condition was reached again, the model exit static pressure was linearly increased at a rate of 100 psia/sec until system instability was indicated. Shown in Figs. 25 and 26 are the model predictions compared to the experimental results, with tabular summaries given in Tables 4 and 5.

The modified model accurately predicted the experimentally determined loss in performance and operability. For performance prediction, the model was within 2.4 percent in compressor

airflow and 1.5 percent in overall compressor pressure ratio over both the 98.6- and 85-percent full speedlines.

The inlet distortion pattern has a significant impact on both compressor performance and operability. For both speeds, the second stage was determined to be the critical stalling stage, since it was the first stage to reach its stability limit (i.e., zero slope of the tangent line on the pressure characteristic). This result is consistent with the results found for the same compressor by Gorrell and Davis (Ref. 14).

In examining compressor operability, the predicted loss in stall margin was 19.25 percent, as compared to an experimental result of 17.27 percent for the 98.6-percent speed. For the 85-percent speed, the effect of the distortion is not as significant, but still accurately predicted. The predicted result agrees favorably to the experimental results, with a loss in stall margin of -0.001 and -1.12 percent, respectively. Tabular summaries of the stall margin results at 98.6- and 85-percent speeds are shown in Tables 6 and 7 (See Appendix B).

The inlet total pressure distortion attenuation was examined for both speeds at two points on the respective speedlines. The attenuation was examined near the operating point and near the stall point. Three axial locations were examined and include the inlet, after the first stage, and after the second stage. Illustrated in Figs. 27a–b are the distortion attenuation for 98.6-percent speed, and illustrated in Figs. 28a–b are the distortion attenuation for 85-percent speed. Near the operating point, the distortion attenuation was predicted within 15 percent of the experimental data for both speeds. Near the compressor instability limit, the distortion attenuation was predicted within 8.5 percent of the experimental data for both speeds. The attenuation was overpredicted for both speeds investigated. This may be attributed to the model's treatment of the exit boundary condition, which was set to a constant Mach number. The experimental rig test used a throttle which was choked, but a circumferential variation in the exit condition probably existed.

The pure parallel model predictions, shown in Figs. 25 – 26, proved to be less accurate than the modified model. For both rotor speeds, the pure parallel model overpredicted the compressor airflow at the instability point. Tabular summaries of the predicted stall points for both speeds are shown in Tables 8 and 9.

The parallel model has reasonable accuracy in the prediction of overall pressure ratio at stall, but has a predicted airflow that is off by as much as 8.6 percent for the 85-percent rotor speed. This result is expected considering that the geometry necessary to adequately simulate the inlet distortion pattern produces a segment angle smaller than the critical angle. As stated previously, the parallel compressor theory is accurate only when the critical angle is greater than 60 deg.

The circumferential mass redistribution and dynamic blade response modifications proved to enhance the predictive capabilities when examining a circumferentially distorted inlet flow. With the classical orifice definition, the orifice flow coefficient,  $K$ , has a lower limit of 0.6, as shown in Fig. 9. For the mass redistribution model, the orifice flow coefficient is represented as the circumferential crossflow coefficient,  $K_c^*$ . A value of 0.6 was used for the  $K_c^*$  term with the results presented above. For some compressor applications, different values for the crossflow coefficient may yield better results.

#### 4.4.2 Hub-Radial Distortion

The next distortion case examined was a pure radial distortion pattern produced by a hub-radial screen. This screen produced a low-pressure region at the hub area of the compressor inlet, while maintaining a relatively clean inlet condition at the tip region of the inlet. A typical hub-radial distortion pattern is shown in Fig. 29. The radial distortion patterns for two corrected rotor speeds, 98.6 percent and 85 percent, are illustrated in Figs. 30 – 31, respectively.

For this application, the model modifications implemented are those that are applicable to a pure radial distortion pattern, which include radial mass redistribution and radial work redistribution. The radial work redistribution scale factors are summarized in Tables 10 and 11 for both the 98.6-percent and 85-percent corrected speeds, respectively.

As with the circumferential distortion cases, the model was initially allowed to reach steady-state at a nominal operating point far from stall for both speeds. Once steady-state operation was achieved, the hub-radial distortion pattern was linearly ramped until it reached its maximum value. The model was then allowed to reach its new steady value. From this new steady value, an aerodynamic throttle at the model exit was closed at a linear rate until model instability was achieved.

For the 98.6-percent and 85-percent speeds, the model predicted compressor performance and operability with relatively good results. The predicted results for compressor performance and operability are illustrated in Figs. 32 – 33, and summarized in Tables 12 and 13.

The predicted stall margin loss,  $\Delta SM$ , for the 98.6-percent speed, was 1.26, as compared to 1.71 for the experimental data. For the 85-percent speed, the stall margin loss was -4.79 for the model and -9.43 for the experimental data. Calculations quantifying both the predicted and experimental instability points are summarized in Tables 14 and 15 for both speeds.

For the 98.6-percent speed case, the model predicted compressor performance within 0.7 percent and 3.3 percent for corrected airflow and overall compressor pressure rise. For the 85-

percent speed case, the predicted compressor performance was within 0.72 percent and 3.4 percent for corrected airflow and overall compressor pressure rise, respectively. For both speeds, the overall predicted compressor performance was good from the operating line up to the stall line.

The radial crossflow coefficient,  $K_r^*$ , was set to 0.005 for the 98.6-percent speed case, and to 0.0065 for the 85-percent speed case. For both speeds, the coefficients were adjusted to calibrate the model to the experimental data.

The inlet total pressure distortion attenuation was examined for both speeds at two points on the respective speedlines. The attenuation was examined near the operating point and near the stall point. Three axial locations were examined and included the inlet, the exit of the first stage, and the exit of the second stage. Illustrated in Figs. 34a–b are the distortion attenuation for 98.6-percent speed, and illustrated in Figs. 35a–b are the distortion attenuation for 85-percent speed. For both speeds, the distortion attenuation was predicted within 2.8 percent for a nominal operating point. Near the instability limit, the distortion attenuation was within 6 percent and 3 percent of the experimental data for 98.6-percent speed and 85-percent speed, respectively. The attenuation was overpredicted for both speeds investigated. Again, this may be attributed to the model's treatment of the exit boundary condition, which was set to a constant Mach number.

#### 4.4.3 Tip-Radial Distortion

The last distortion case examined is a pure radial pattern for the 85-percent corrected speed only. Insufficient information was available for the investigation of the 98.6-percent speed for the tip-radial case. The tip-radial screen produces a low-pressure region at the blade tip region of the compressor inlet, while a relatively clean inlet flow condition is maintained at the hub region of the compressor inlet. A typical tip-radial screen is shown in Fig. 36 with a typical distortion pattern produced by this screen shown in Fig. 37. The radial work redistribution scale factors are identical to those used for the 85-percent speed hub-radial case (See Table 11).

As with the circumferential and hub-radial distortion cases, the model was initially allowed to reach steady state at a nominal operating point far from stall. Once steady state had been achieved, the tip-radial distortion pattern was linearly ramped until it reached its maximum value. The model was then allowed to reach its new steady value. From this new steady value, an aerodynamic throttle at the model exit was closed at a linear rate until model instability was achieved.

The 85-percent corrected speed was examined with the tip-radial distortion pattern shown in Fig. 38. The predicted results from the modified model are shown in Fig. 39 and summarized in Table 16. The predicted stall margin loss,  $\Delta SM$ , for this case was 8.46, as compared to 5.98 for the experimental data.

The predicted compressor performance was within 1.43 percent and 0.61 percent for corrected airflow and overall compressor pressure ratio as compared to experimental data. The value for the radial crossflow coefficient,  $K_r$ , that was used for the tip-radial distortion case was 0.005. This coefficient was adjusted to calibrate the model to the experimental data.

The inlet total pressure distortion attenuation was examined for the 85-percent speed at two points on the speedline. The attenuation was examined near the operating point and near the stall point. Three axial locations were examined including the inlet, the exit of the first stage, and the exit of the second stage. Illustrated in Figs. 40a–b are the distortion attenuation for 85-percent speed. For a nominal operating point, the distortion attenuation was predicted within 10 percent of the experimental data. Near the compressor instability limit, the distortion attenuation was predicted within 11.5 percent of the experimental data. The attenuation was overpredicted for the speed investigated. This may be attributed to the model's treatment of the exit boundary condition, which was set to a constant Mach number. In all cases, the experimental rig test used a choked throttle, but a radial variation in the exit condition probably existed.

## 5.0 SUMMARY

The objective of this research was to modify and calibrate a one-dimensional dynamic compression system model, DYNTECC, to more accurately simulate compressor operation with steady, nonuniform inlet flow. The modifications were based upon parallel compressor theory and modeled both circumferential and radial flow effects of distorted inlet flow. The circumferential modifications included circumferential mass redistribution and dynamic blade response. The radial modifications included radial mass redistribution and radial work redistribution.

The circumferential mass redistribution allowed mass transport between adjacent circumferential segments within the compressor section. The mass redistribution considered mass transport through the rotor-stator gap, and utilized a simple orifice flow analogy to obtain an algebraic expression. The dynamic blade response modification modeled the blade's response to inlet circumferential pressure distortions. A dynamic lag ratio, DLR, was used to damp the model's response to a flow disturbance. DYNTECC uses quasi-steady stage characteristics, and the DLR compensated for the finite response time, or dynamic response, of the rotor blade.

The radial mass redistribution is based on a simplification of the radial momentum equation. The mass redistribution model used began with the Bernoulli equation and included an additive term that is a function of terms such as the viscous and centrifugal forces. The radial mass redistribution model used by Kimzey (Ref. 10) uses a multiplying crossflow coefficient as well as a separate force term that included the viscous and centrifugal forces. A simpler model was used due to the lack of theoretical or empirical information concerning the magnitude of Kimzey's radial force term,  $FR$ .

Additional radial modifications include a radial work redistribution model. This model utilized a simple approach of specifying scale factors for the stage characteristics to more accurately account for the compressor blade loading. Work redistribution scale factors were used to adjust the pressure and temperature stage characteristics for each radial segment. This work redistribution adjusted the characteristics to accurately reflect experimental data.

The model was first compared to experimental results for a low-aspect-ratio compressor with a clean inlet at two corrected rotor speeds, 98.6 percent and 85 percent. For the 98.6-percent speed, both compressor performance predictions were within 1 and 0.2 percent for compressor corrected airflow and overall pressure ratio, respectively. For the 85-percent speed, the model performance predictions were within 0.4 and 0.65 percent for corrected airflow and overall compressor pressure ratio, respectively. In terms of predicted instability, both speeds were within 1 and 0.17 percent for corrected airflow and compressor pressure ratio at stall.

The modified model was calibrated to experimental results for the same compressor for several distorted inlet cases. The distorted cases examined were total pressure inlet distortions and included a one/revolution circumferential distortion, a hub-radial distortion, and a tip-radial distortion. For the first two distortion cases, two corrected rotor speeds were examined, 98.6 percent and 85 percent. For the tip-radial or last distortion case, only the 85-percent corrected rotor speed was used.

For the one/revolution circumferential distortion case, two modifications were implemented, including the circumferential mass redistribution and the dynamic blade response. The modified model predicted performance to within 2.4 percent for corrected airflow and 1.5 percent for overall compressor pressure ratio for both the 98.6- and 85-percent rotor speeds. For the 98.6-percent speed, the modified model predicted the loss in compressor stall margin,  $\Delta SM$ , to be 19.25 as compared to the experimental value of 17.27. For the 85-percent speed case, the modified model predicted the stall margin loss to be -0.001 as compared to an experimental value of -1.12. For both speeds, the distortion attenuation was examined, which saw an overprediction of the distortion attenuation.

Additionally, for the one/revolution distortion cases, a model based on the classic parallel compressor theory was compared to experimental data. For a 98.6-percent corrected rotor speed, the parallel model predicted the compressor stall point within 0.96 percent for corrected airflow and 0.86 percent for overall compressor pressure ratio, as compared to the experimental data. For the 85-percent corrected rotor speed, the parallel model predicted the compressor stall point within 8.63 percent for corrected airflow and 1.19 percent for overall compressor pressure ratio, as compared to the experimental data.

For a hub-radial distortion case, two modifications were implemented, including the radial mass redistribution and the radial work redistribution. For the 98.6-percent corrected rotor speed, the modified model predicted compressor performance within 0.7 percent for corrected airflow and 3.3 percent for overall compressor pressure ratio. For the 85-percent rotor speed, the modified model predicted compressor performance within 0.72 percent for corrected airflow and 3.4 percent for overall compressor pressure ratio. For the 98.6-percent speed, the modified model predicted the loss in stall margin to be 1.26 as compared to 1.71 for the experimental data. For the 85-percent rotor speed, the modified model predicted the loss in stall margin to be -4.79 as compared to a value of -9.43 for the experimental data.

The last distortion case that was examined was a tip-radial pattern at an 85-percent corrected rotor speed. The modified model predicted compressor performance within 0.74 percent for corrected airflow and 0.61 percent for overall compressor pressure ratio. The modified model predicted the loss of compressor stall margin to be 8.46 as compared to 5.98 for the experimental data.

## 6.0 CONCLUSIONS

Overall, the modified model proved to predict the compressor performance and operability with a reasonable level of accuracy. The circumferential modifications provided excellent agreement with the experimental data with a significant improvement over the classic parallel compressor theory. The addition of the modifications addresses the limitation of the critical angle in the parallel compressor theory. Without the limitation of the critical angle, compressor performance can be examined with more complex inlet distortion patterns.

For the circumferential distortion cases, the modified model provided good predictions of compressor performance and operability for both speeds with little adjustment or calibration of the model. The dynamic blade response was based solely on the reduced frequency of the inlet distortion and of the velocity of the circumferential mass redistribution. The circumferential mass redistribution was modeled by a simple orifice analogy allowing the selection of the coefficient to be soundly based. The assumptions of high Reynolds number and pronounced vena contracta provide a sound basis for the selection of 0.6 for the coefficient. Using this coefficient, the modified model proved to be an excellent predictor of the experimental data.

The single area that proved to be overpredicted was the distortion attenuation. Both near the operating point and near the compressor stability limit, the model overpredicted the attenuation, especially at the exit of the second stage. Thus, the overprediction was progressively worse as analysis proceeded axially through the compressor. This may be attributed to the model's treatment of the exit boundary condition, which was set to a constant Mach number. The experimental test rig used a throttle which was choked, but a circumferential variation in the exit condition probably existed.



The radially modified model provided mixed results when both the hub- and tip-radial distortions were examined. The radial work redistribution model was simple with scale factors based solely on experimental interstage data. The radial mass redistribution model was based on a simplification of the radial momentum equation. While the circumferential model was also based on a simplified momentum equation, the resulting orifice analogy has numerous empirical results on which a flow coefficient can be based. With the radial model, no applicable empirical results or experimental investigations were found, unlike the circumferential mass redistribution model. Without the ability to quantify parameters such as the radial viscous and centrifugal forces, the mass flow in the radial direction had to be calibrated to experimental data. Even with the relatively simple radial model, the calibrated compressor performance and operability compared favorably with the experimental data. These results are encouraging considering the lack of refinement of the radial models.

## **7.0 RECOMMENDATIONS FOR FUTURE WORK**

Foremost in the recommendations, additional experimental data are needed to further examine the modified model. These experimental data should include both simple circumferential and radial pressure and temperature distortions, as well as more complex patterns. These complex patterns could potentially be a combination of radial and circumferential distortions, and include a combination of pressure and temperature.

Additionally, more compressor configurations should be considered. The current research examined a low-aspect-ratio, two-stage fan, while Kimzey's (Ref. 10) efforts focused on multistage, high-pressure compressors similar to core compressors found in aircraft turbine engines. Future investigations should include a variety of compressor configurations including large numbers of stages, varying overall compressor geometries (i.e., large and small diameter compressors), and varying interstage geometries. The interstage geometries should include varying blade row gaps, swept blades, and interstage bleeds.

Because of the mixed results of this research, a better radial mass redistribution model is recommended to provide more accurate levels of prediction. Kimzey (Ref. 10) referred to the model in 1977 as crude, and called for a more accurate model. The existing radial mass redistribution model does not adequately address the complex flow conditions found in the radial direction.

An alternative to the pursuit of a more accurate radial mass redistribution model is the investigation of a multidimensional model (i.e., two- or three-dimensional models). These types of multidimensional, dynamic models could greatly increase the accuracy of the predicted compressor performance and operability. Additionally, a greater understanding of the flow interactions within small segments of the compressor could be analyzed. An example of this type of multidimensional

dynamic code was presented by Hale, Davis, and Kneile (Ref. 17). One negative aspect of such models is that a considerably greater amount of computer resources are necessary to execute them. The one-dimensional dynamic simulation presented here can be run on a desktop personal computer, while the multidimensional models require a workstation as a minimum platform.

## REFERENCES

1. Longley, J. P. and Greitzer, E. M. "Inlet Distortion Effects in Aircraft Propulsion System Integration." Advisory Group for Aerospace Research & Development Lecture Series, AGARD-LS-183, May 1992.
2. Hale, A. A. and Davis, M.W., Jr. "DYNAMIC Turbine Engine Compressor Code, DYNTECC — Theory and Capabilities." AIAA/SAE/ASME/ASEE 28th Joint Propulsion Conference, AIAA-92-3190, Nashville, TN, July 1992.
3. Korn, J. A. "Estimated Effect of Circumferential Distortion on Axial Compressors Using Parallel Compressor Theory and Dynamic Stall Delay." AIAA 12th Aerospace Sciences Meeting, AIAA-74-233, Washington, D.C., January 1974.
4. Goethert, B. H. and Reddy, K. C. "Unsteady Aerodynamics of Rotor Blades of a Compressor Under Distorted Flow Conditions." AGARD Paper Presentation, Silver Springs, MD, September 1970.
5. Steenken, W. G. "Modeling Compression Component Stability Characteristics — Effects of Inlet Distortion and Fan Bypass Duct Disturbances." Advisory Group for Aerospace Research & Development Conference Proceedings, AGARD-CP-324, February 1983.
6. Tesch, W. A. and Steenken, W. G. "Blade Row Dynamic Digital Compressor Program Volume II — J85 Circumferential Distortion Redistribution Model, Effect of Stator Characteristics, and Stage Characteristics Sensitivity Study." National Aeronautics and Space Administration Contractor Report, NASA-CR-134953, July 1978.
7. Mazzawy, R. S. "Multiple Segment Parallel Compressor Model for Circumferential Flow Distortion." *Journal of Engineering for Power*, April 1977.
8. Mazzawy, R. S. and Banks, G. A., "Circumferential Distortion Modeling of the TF30-P-3 Compression System." National Aeronautics and Space Administration Contractor Report, NASA-CR-135124, January 1977.

9. Mazzawy, R. S. and Banks, G. A. "Modeling and Analysis of the TF30-P-3 Compressor System with Inlet Pressure Distortion." National Aeronautics and Space Administration Contractor Report, NASA-CR-134996, April 1976.
10. Kimzey, W. F. "An Analysis of the Influence of Some External Disturbances on the Aerodynamic Stability of Turbine Engine Axial Flow Fans and Compressors." AEDC-TR-77-80, August 1977.
11. Davis, M. W. Jr. "Parametric Investigation into the Combined Effects of Pressure and Temperature on Compression System Stability." AIAA/SAE/ASME/ASEE 27th Joint Propulsion Conference, AIAA-91-1895, Sacramento, CA, June 1991.
12. Reddy, K. C. and Sudheer, N. N. "Compressor and Turbine Models - Numerical Stability and Other Aspects." AEDC-TR-85-5, April 1985.
13. Baumeister, T., Avallone, E. A., and Baumeister, T. III, ed. *Mark's Standard Handbook for Mechanical Engineers*. McGraw-Hill Book Company, New York, 1978 (Eighth Edition).
14. Gorrell, S. E. and Davis, M. W. Jr. "Application of a Dynamic Compression System Model to a Low Aspect Ratio Fan: Casing Treatment and Distortion." AIAA/SAE/ASME/ASEE 29th Joint Propulsion Conference, AIAA-93-1871, Monterey, CA, June 1993.
15. "Gas Turbine Engine Inlet Flow Distortion Guidelines." Society of Automotive Engineers Aerospace Recommended Practice, ARP 1420, March 1978.
16. Fox, R. W. and McDonald, A. T. *Introduction to Fluid Mechanics*.: John Wiley & Sons, New York, 1985 (Third Edition).
17. Hale, A. A., Davis, M. W. Jr., and Kneile, K. R. "Turbine Engine Analysis Compressor Code: TEACC, Part I: Technical Approach and Steady Results." 32nd Aerospace Sciences Meeting, AIAA-94-0148, Reno, NV, January 1994.
18. Chamblee, C. E. "Some Refinements and Applications of the Multi-Stage Axial Flow Compressor Time-Dependent Mathematical Modeling Technique." Master's Thesis, University of Tennessee, Knoxville, 1979.

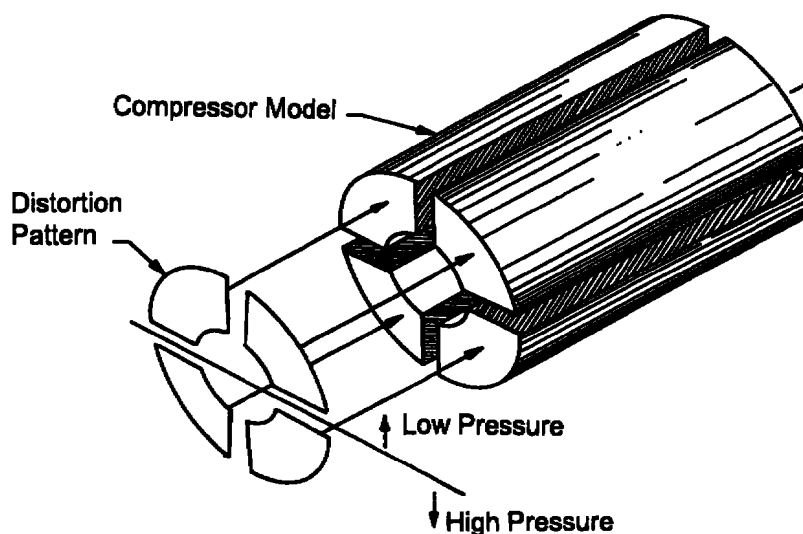


**Figure 1. Example of the parallel compressor theory concept with circumferential segments and an applied inlet distortion (Ref. 2).**

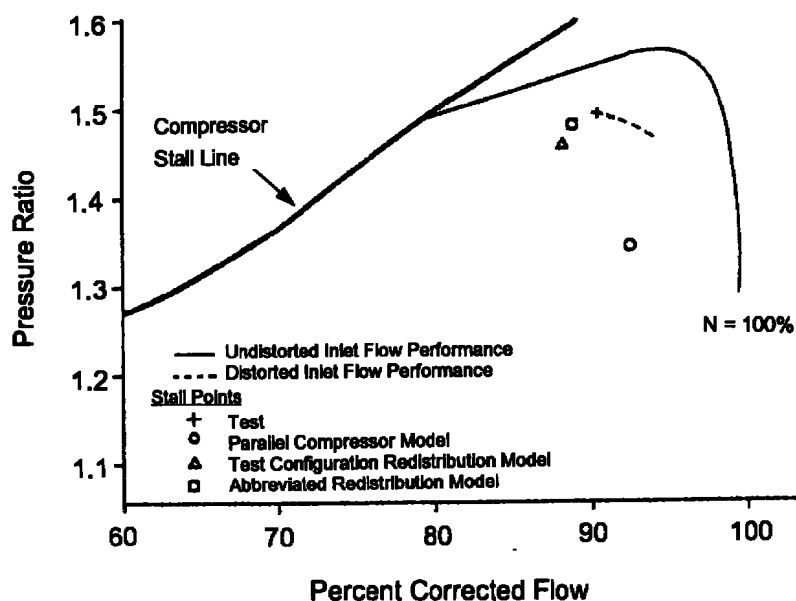


**Figure 2. Results from Steenken's research showing the predictions of the modified model and the pure parallel model versus experimental data (Ref. 5).**

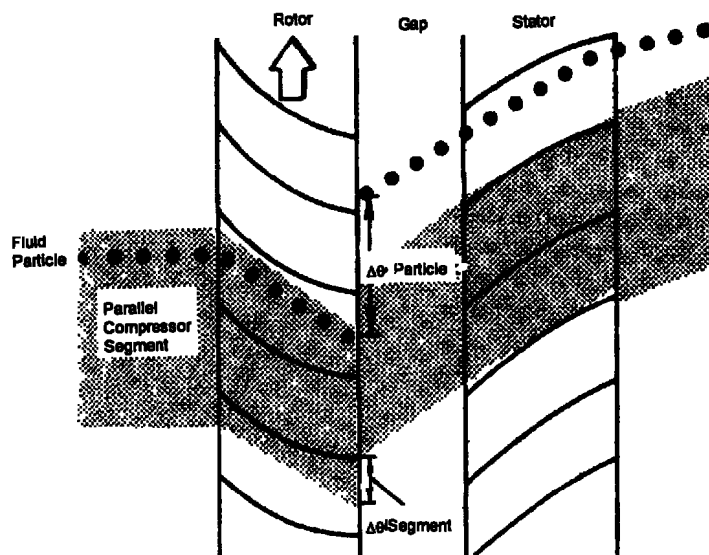
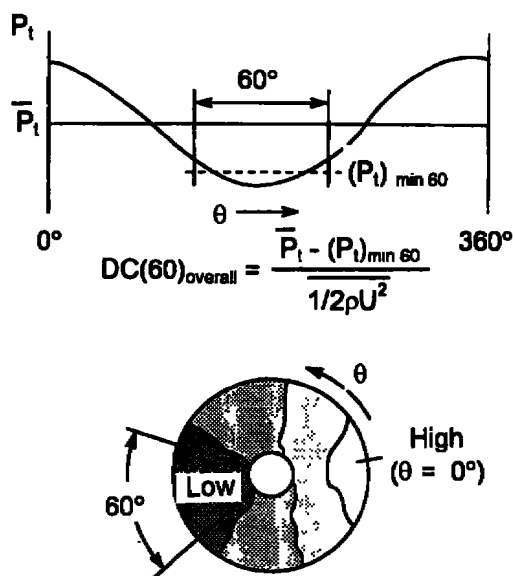


**Figure 3. Illustration of the angular displacement of the circumferential segments through the rotor, utilized in Mazzawy's compressor model (Ref. 7).**



**Total Pressure Contour Plot**

**Figure 4. Example of distortion index for a circumferential total pressure distortion pattern (Ref. 1).**

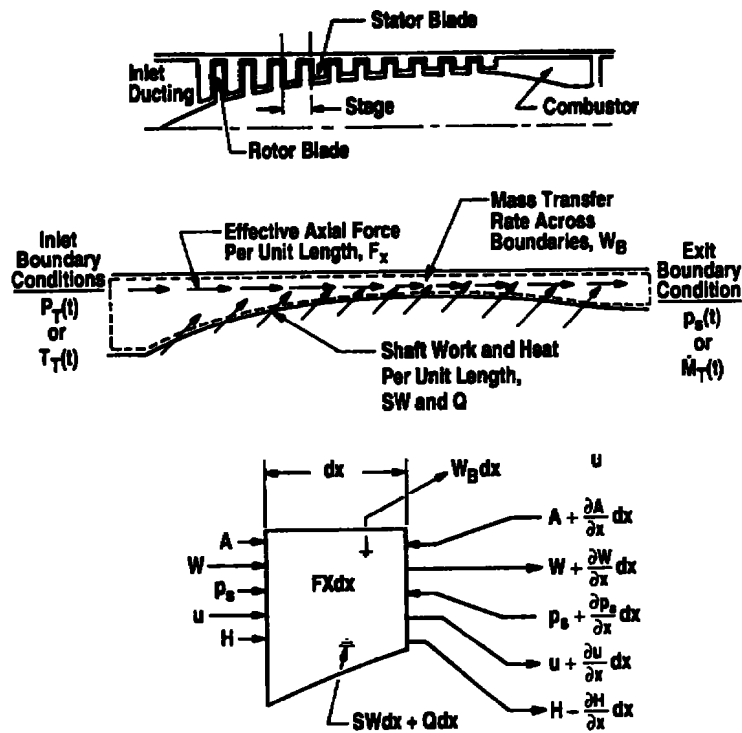


Figure 5. Schematic of the physical compression system and the 1-D control volume concepts of the 1-dimensional model (Ref. 10).

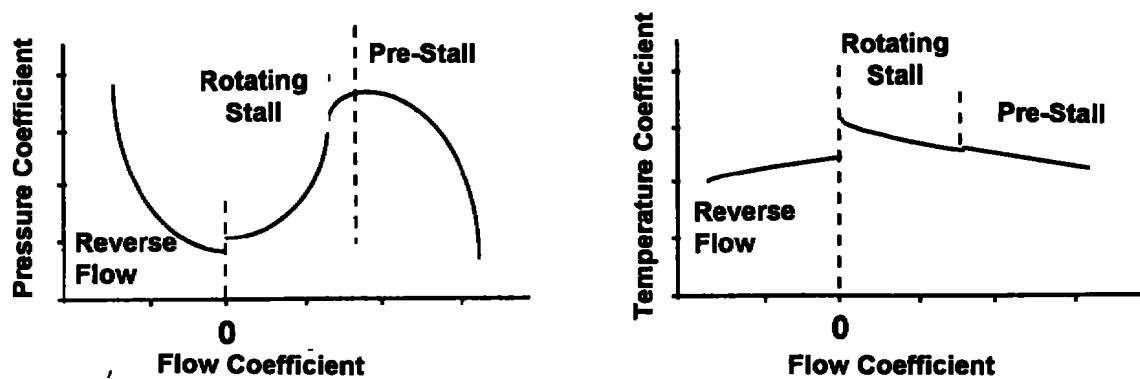
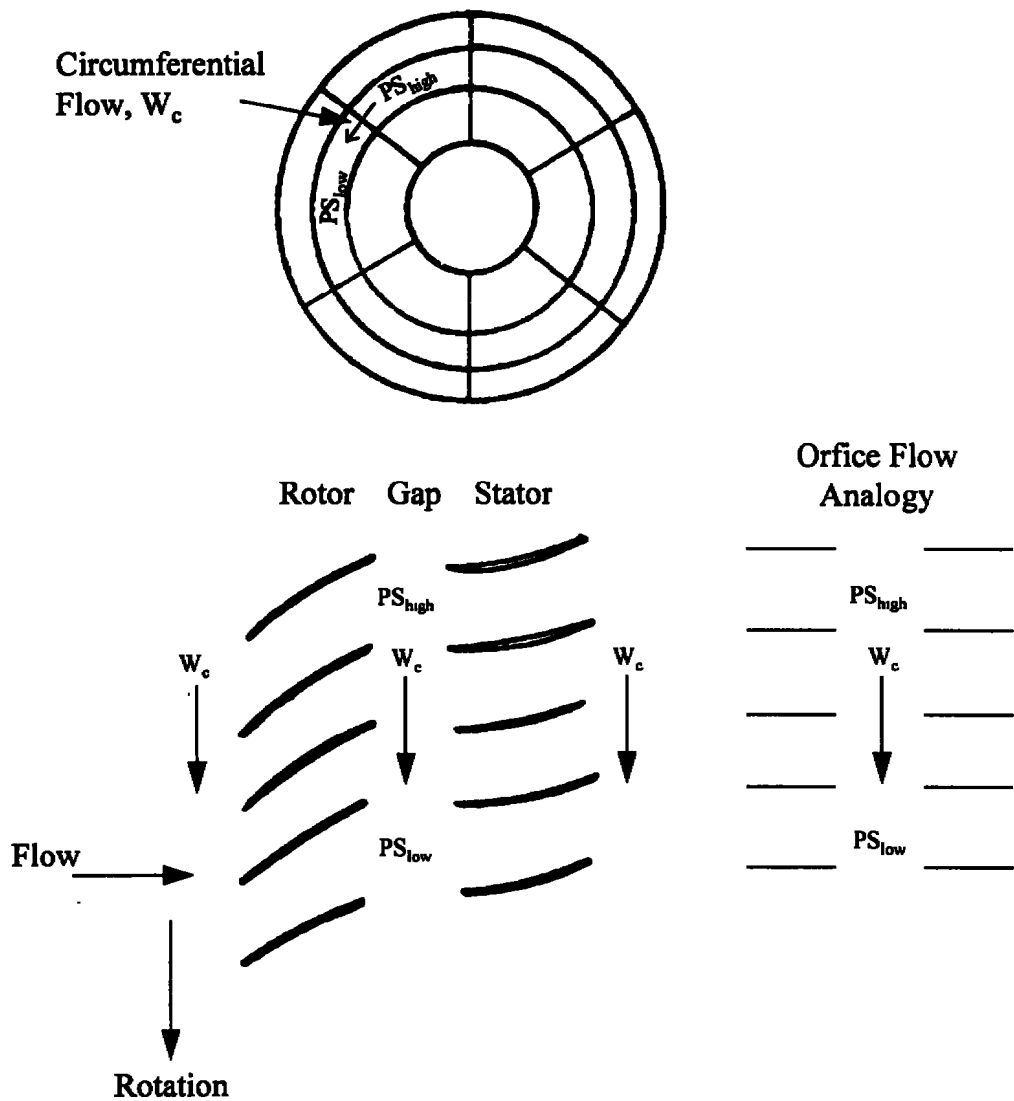


Figure 6. Example of compressor quasi-steady stage characteristics.



**Figure 7. Illustration of the circumferential crossflow model with the orifice flow analogy (Ref. 10).**

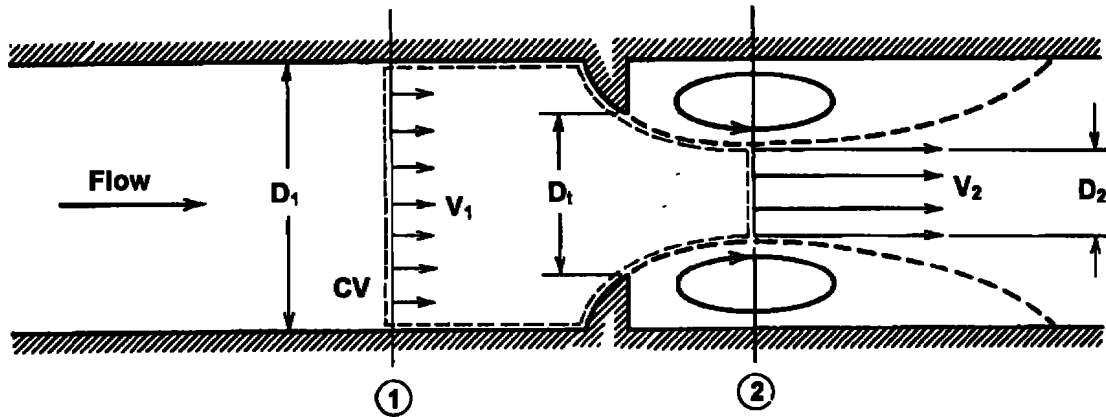


Figure 8. Classical orifice model illustration (Ref. 16).

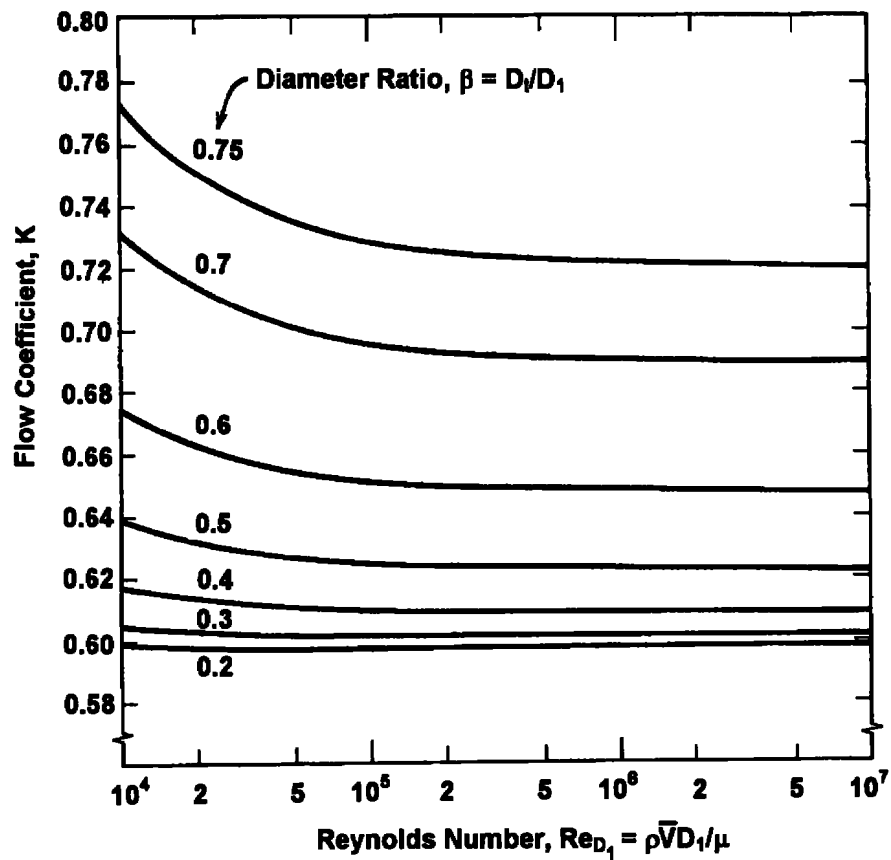


Figure 9. Plot of the flow coefficient,  $K$ , for the classical orifice model (Ref. 16).



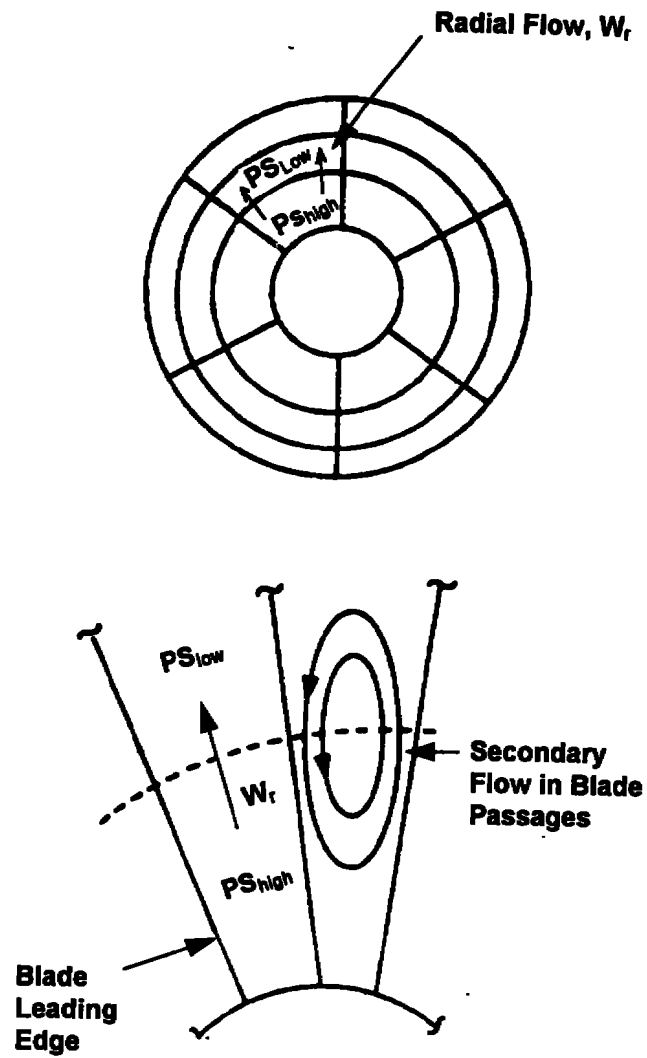
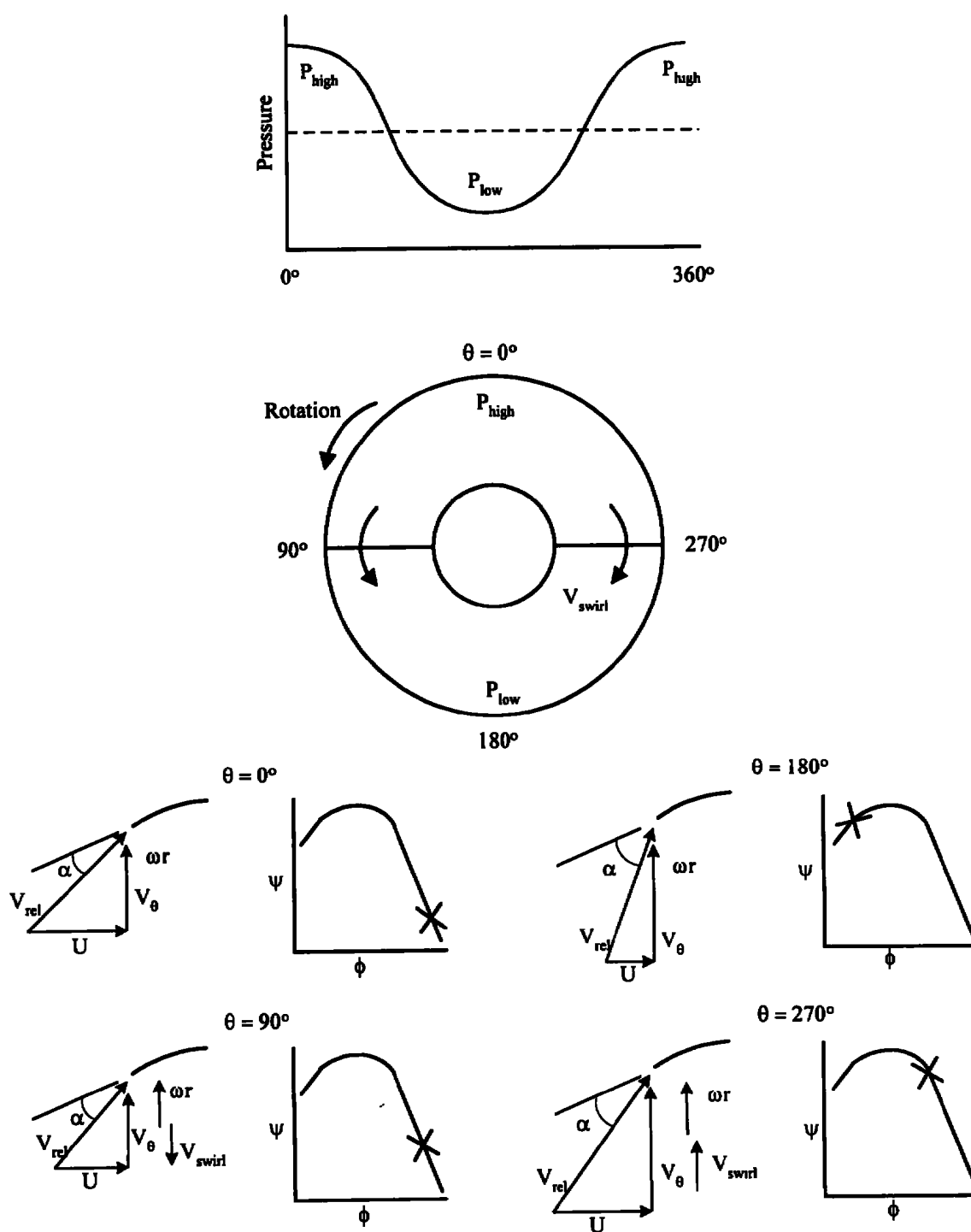


Figure 10. Illustration of the radial crossflow model (Ref. 10).



**Figure 11. 180-deg circumferential distortion and its effects on flow velocity relative to the rotor blade (Ref. 10).**

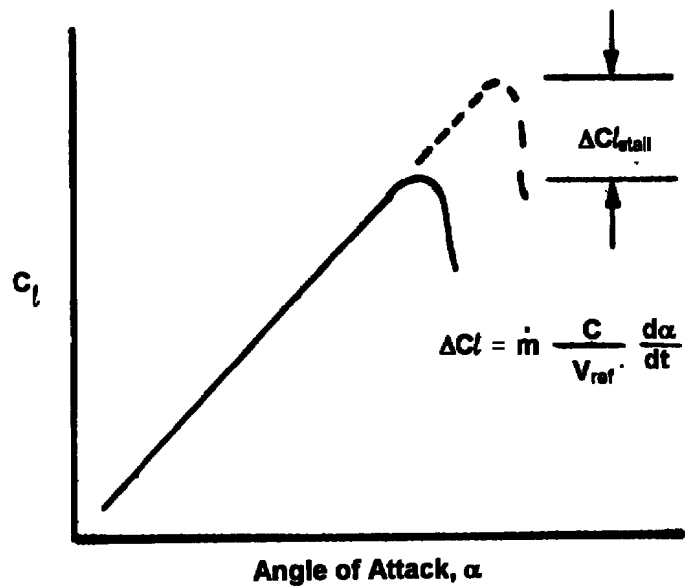


Figure 12. Rotor blade coefficient of lift as blade angle of attack varies (Ref. 10).

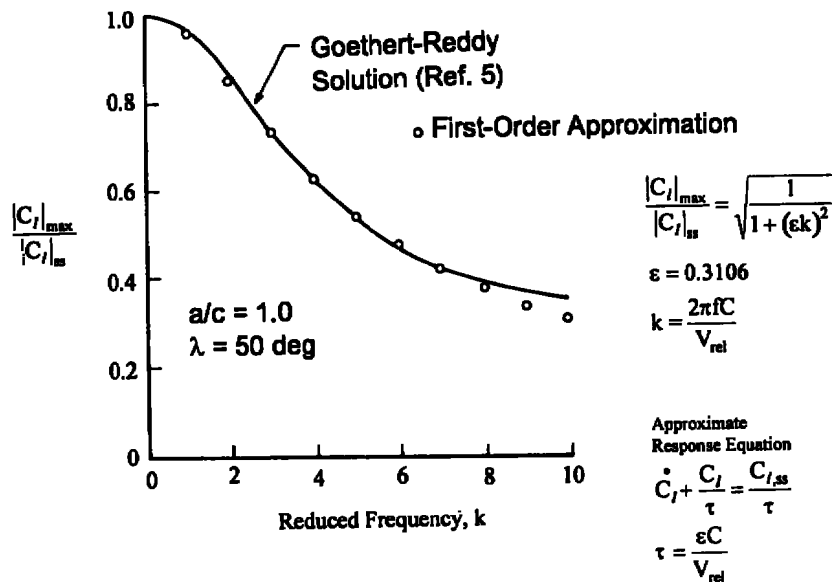
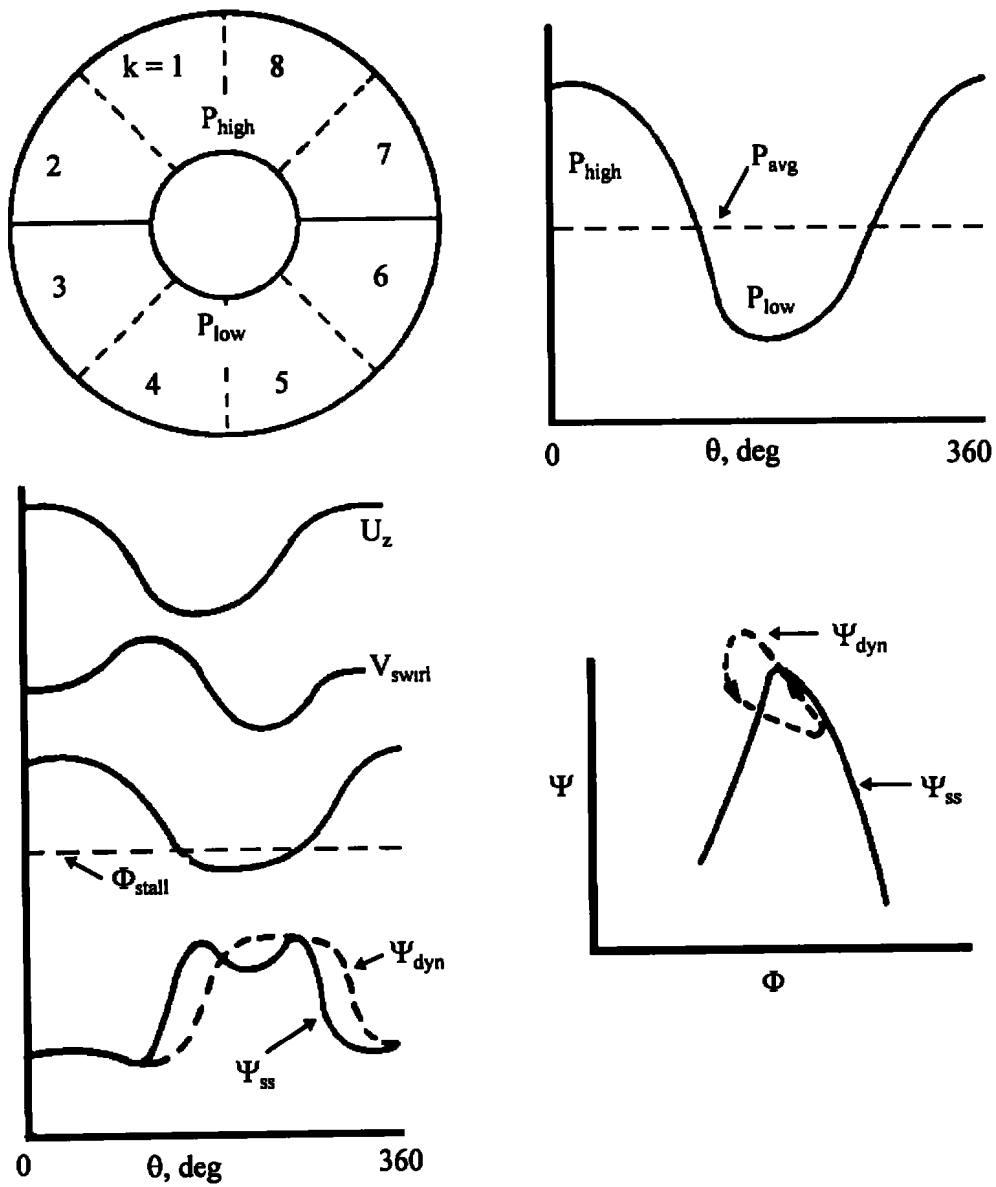
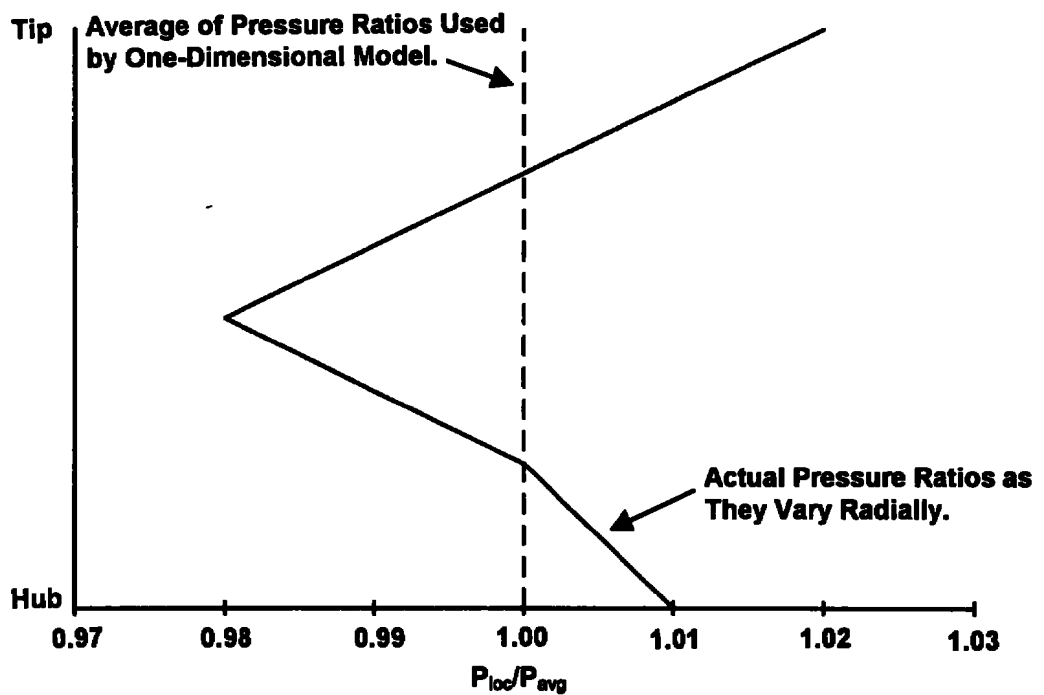


Figure 13. Unsteady lift coefficient magnitude ratio (Ref. 10).



**Figure 14. Unsteady blade response to circumferentially nonuniform flow conditions (Ref. 10).**



**Figure 15. Illustration of work redistribution concept with radial variation of pressure ratios.**

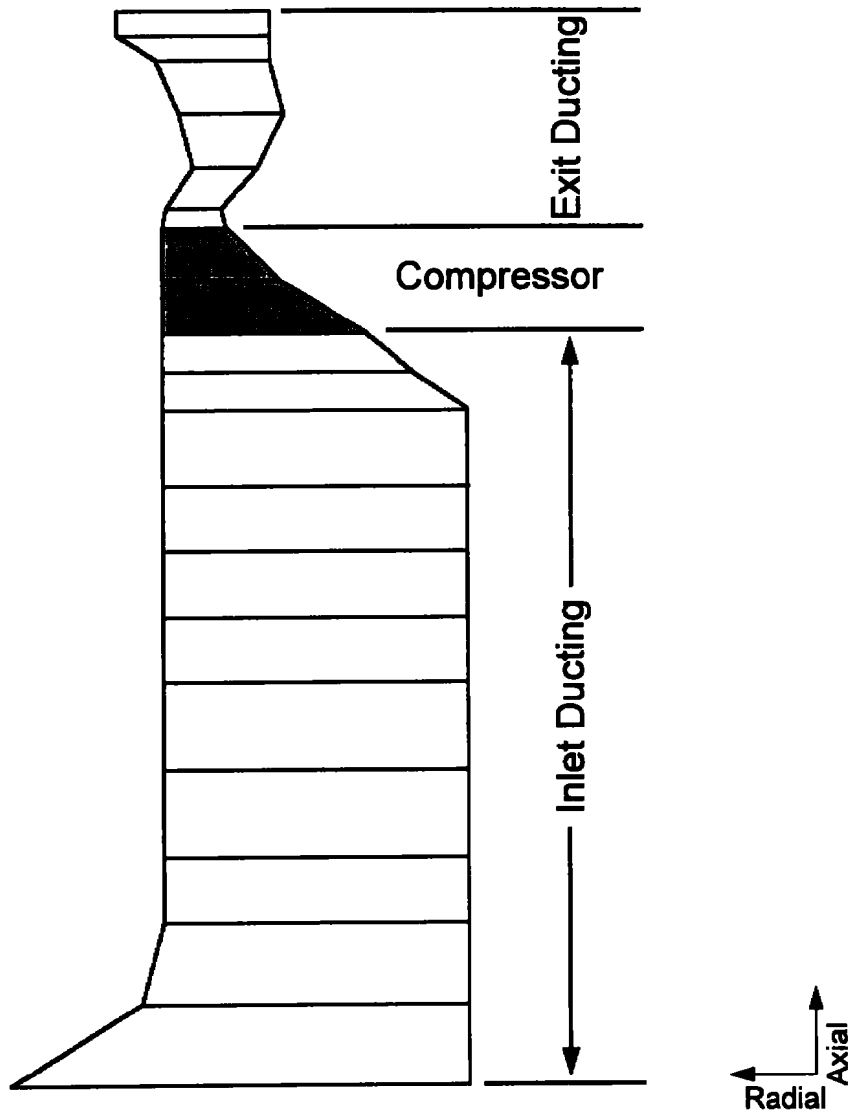
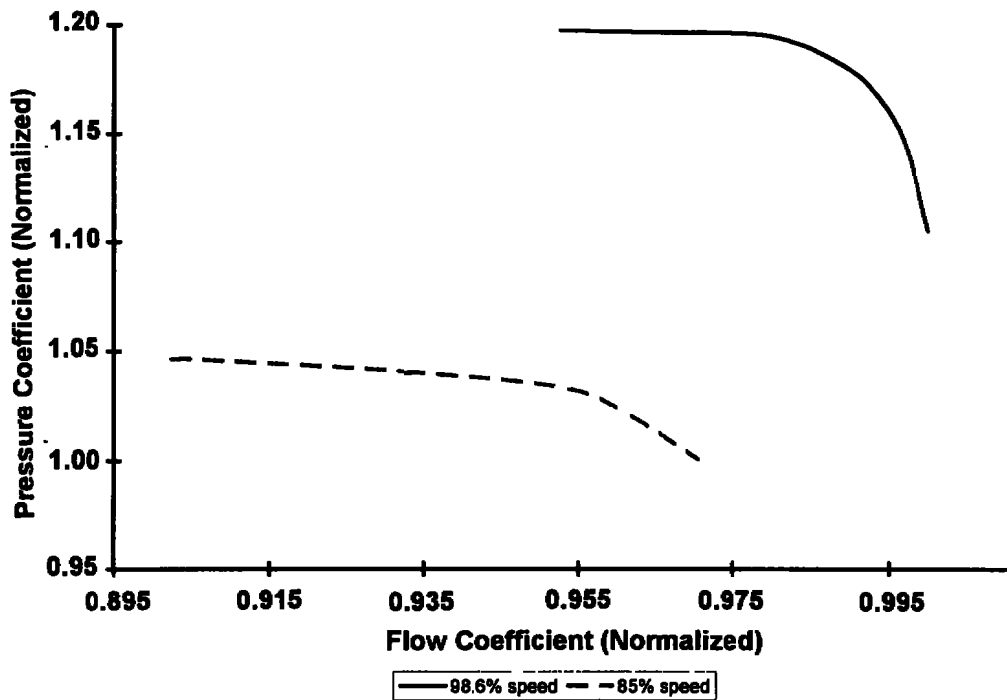
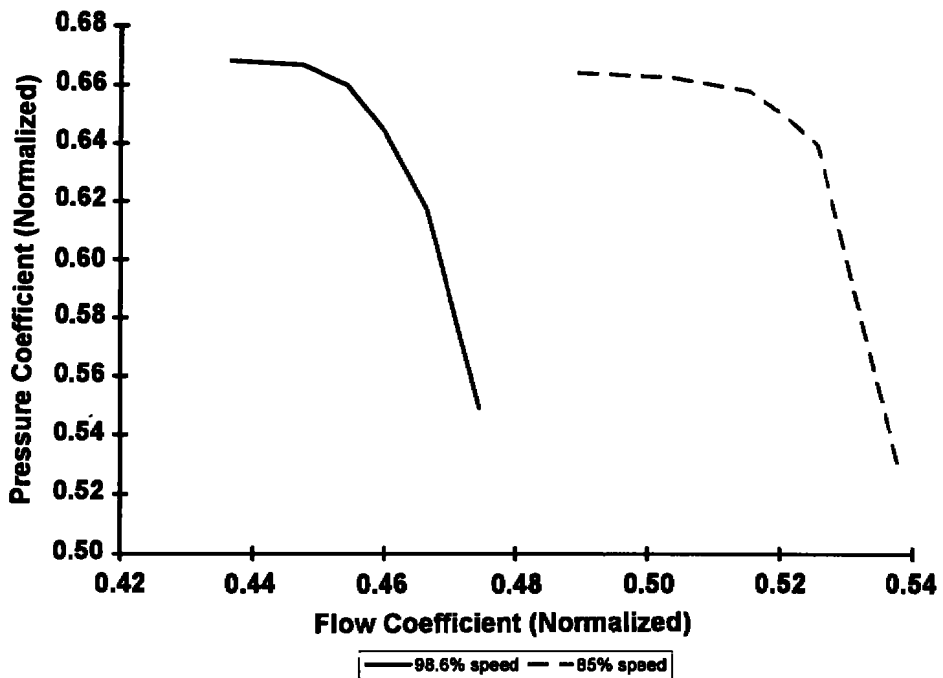


**Figure 16. Compression system model geometry with axial segments.**

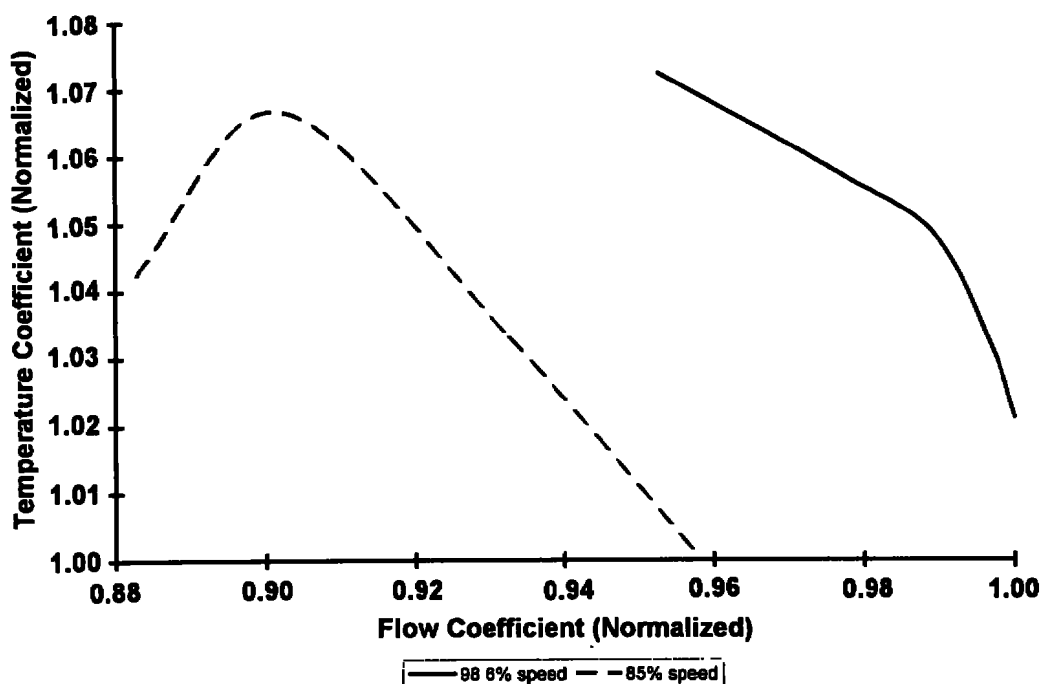


a. Normalized first-stage compressor characteristics

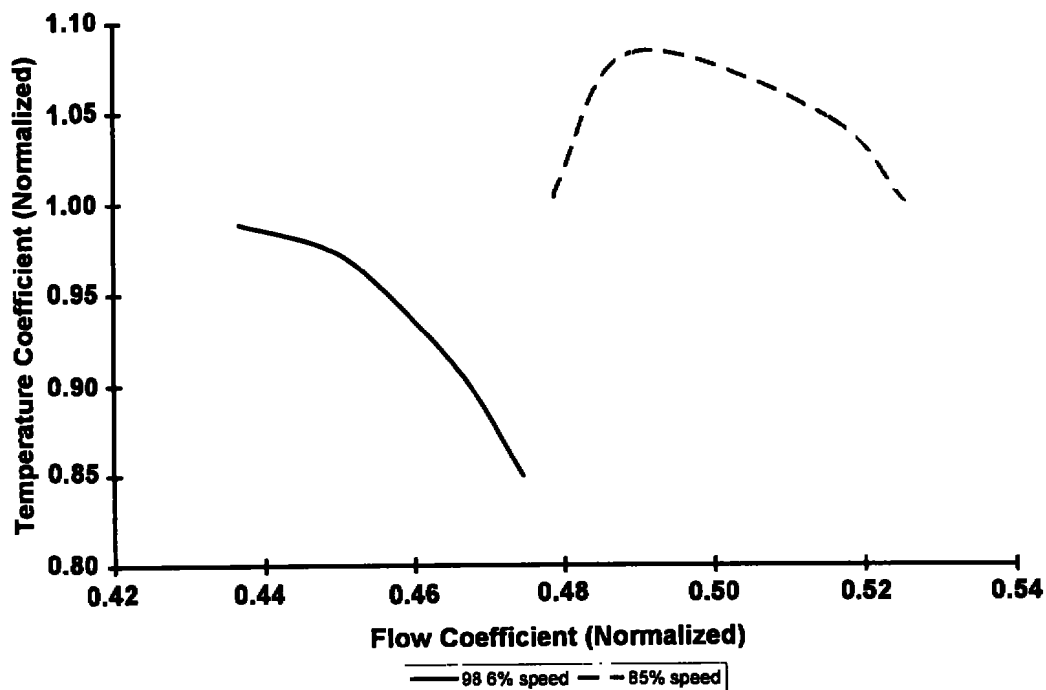


b. Normalized second-stage compressor characteristics

Figure 17. Pressure coefficient as a function of flow coefficient.



a. Normalized first-stage compressor characteristics



b. Normalized second-stage compressor characteristics

Figure 18. Temperature coefficient as a function of flow coefficient.



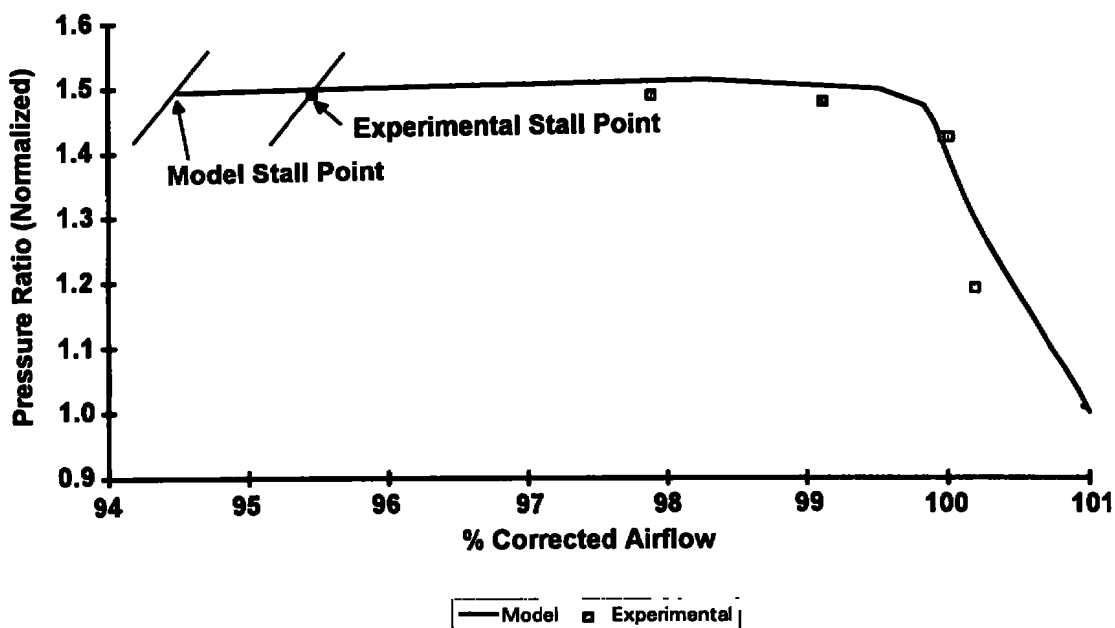


Figure 19. Clean inlet performance model prediction and experimental data (98.6-percent rotor speed).

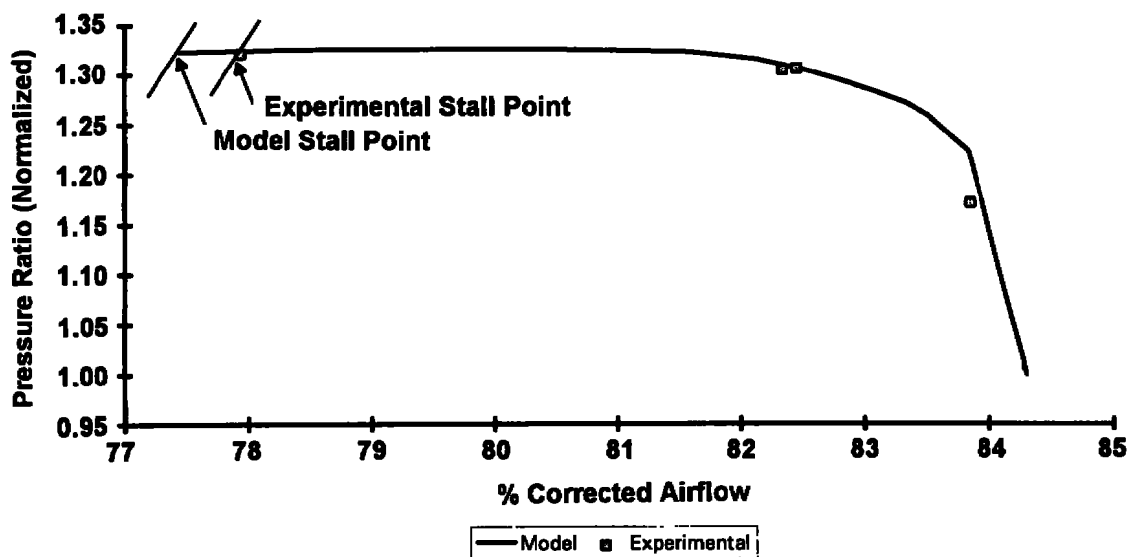
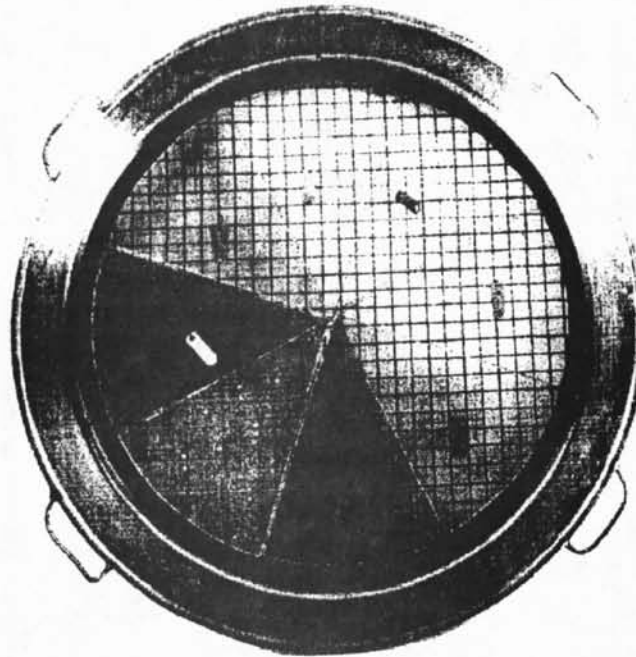
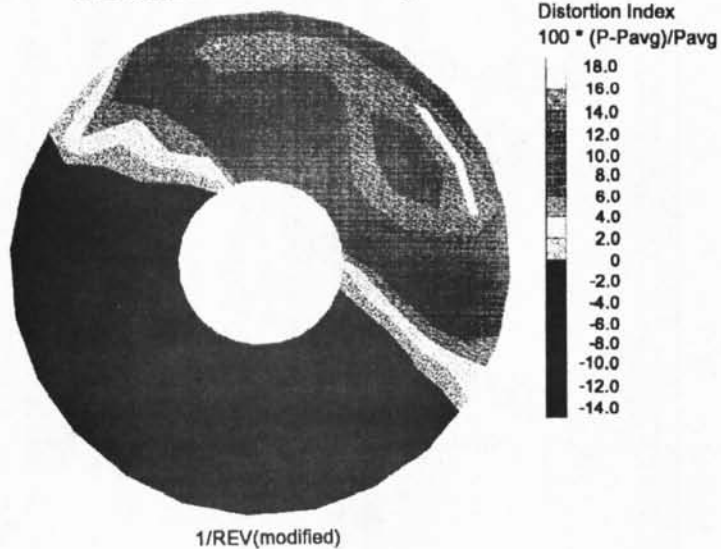


Figure 20. Clean inlet performance model prediction and experimental data (85-percent rotor speed).



**Figure 21. One/revolution total pressure distortion screen [Courtesy of Compressor Research Facility, Wright-Patterson Air Force Base].**

**Distortion Inlet Total Pressure Contours  
% Deviation from Face Average**



**Figure 22. Typical inlet total pressure pattern produced by a one/revolution distortion screen [Courtesy of Compressor Research Facility, Wright-Patterson Air Force Base].**

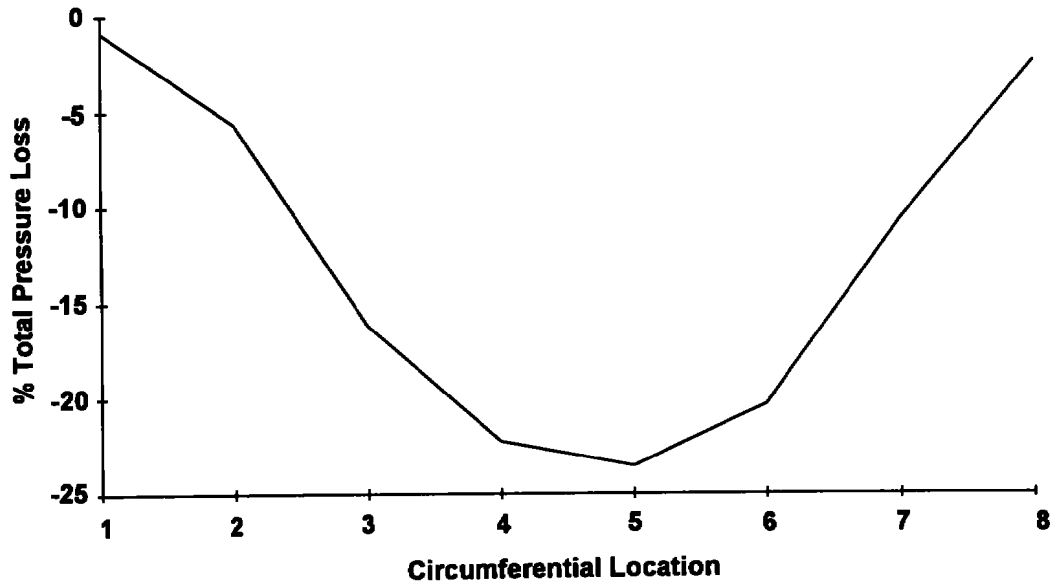


**Figure 23. Total pressure distortion pattern produced by the one/revolution distortion screen at 98.6-percent corrected rotor speed.**

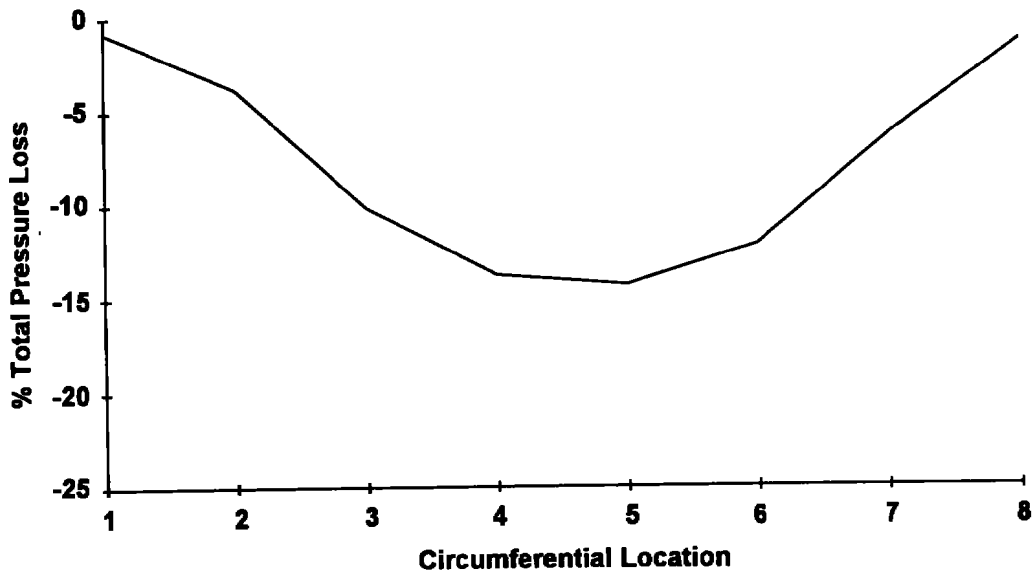


**Figure 24. Total pressure distortion pattern produced by the one/revolution distortion screen at 85-percent corrected rotor speed.**

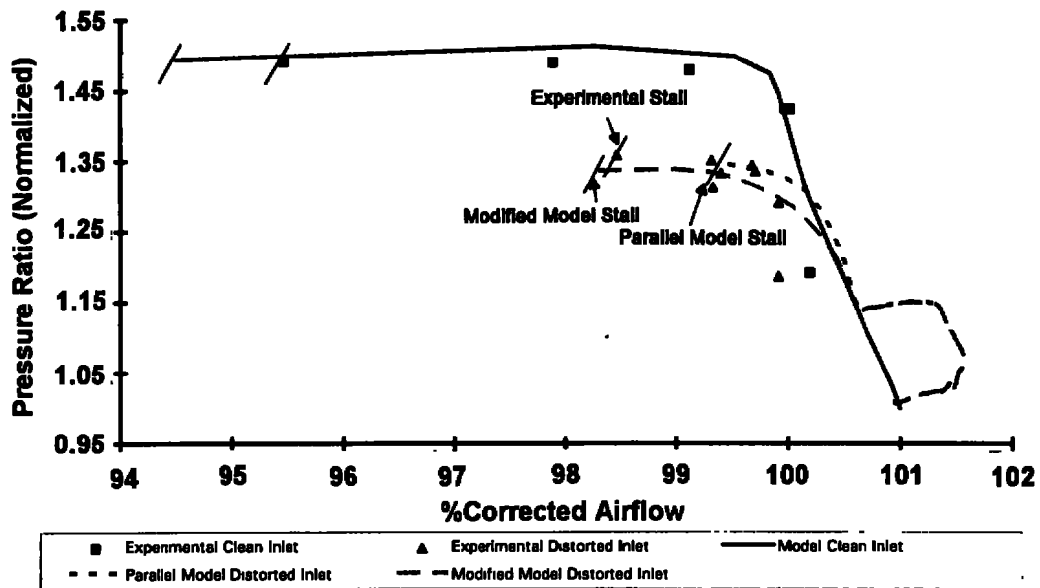


Figure 25. Compressor performance prediction for one/revolution circumferential distortion screen at 98.6-percent corrected rotor speed.

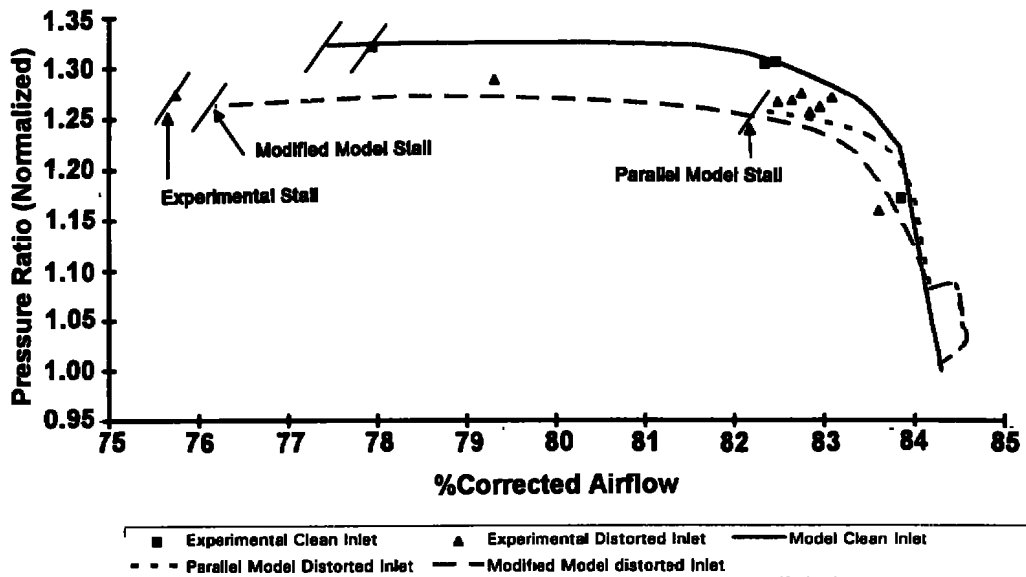
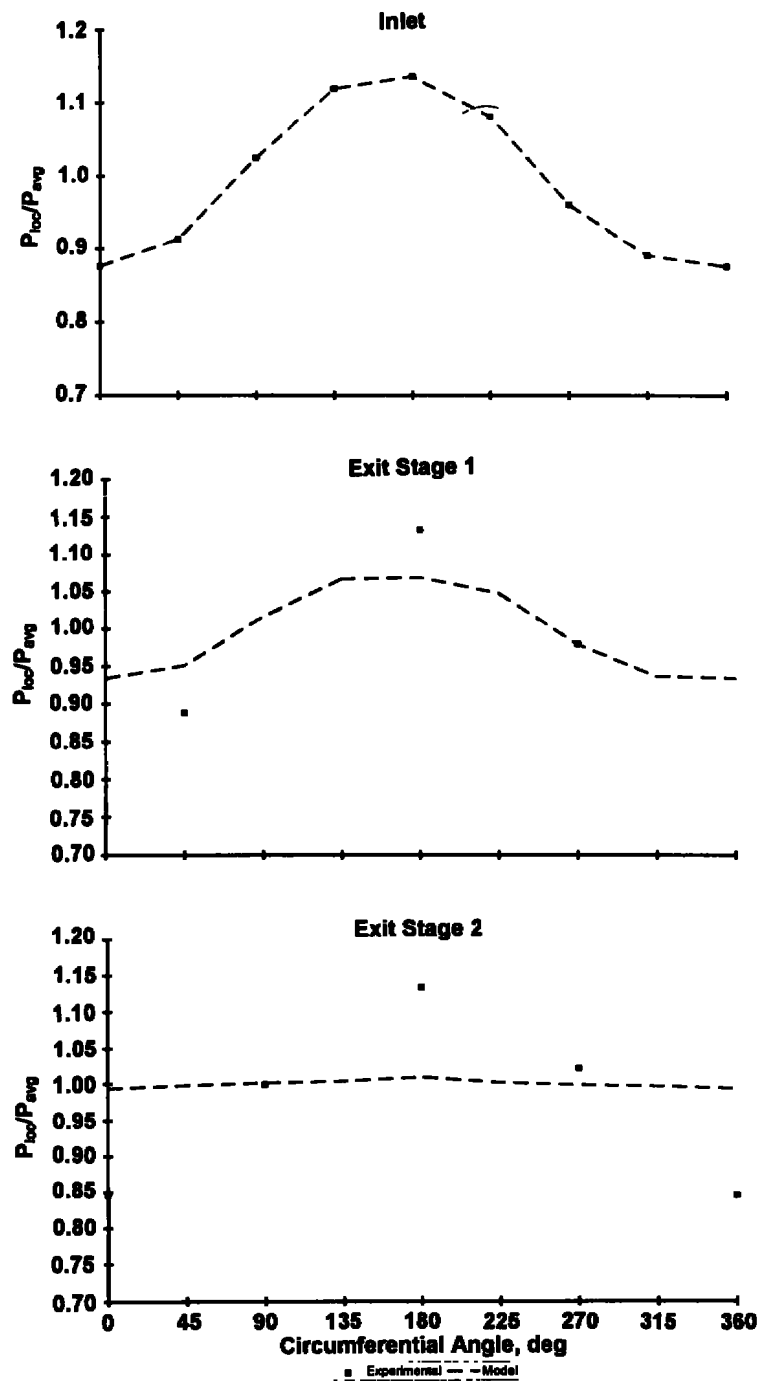
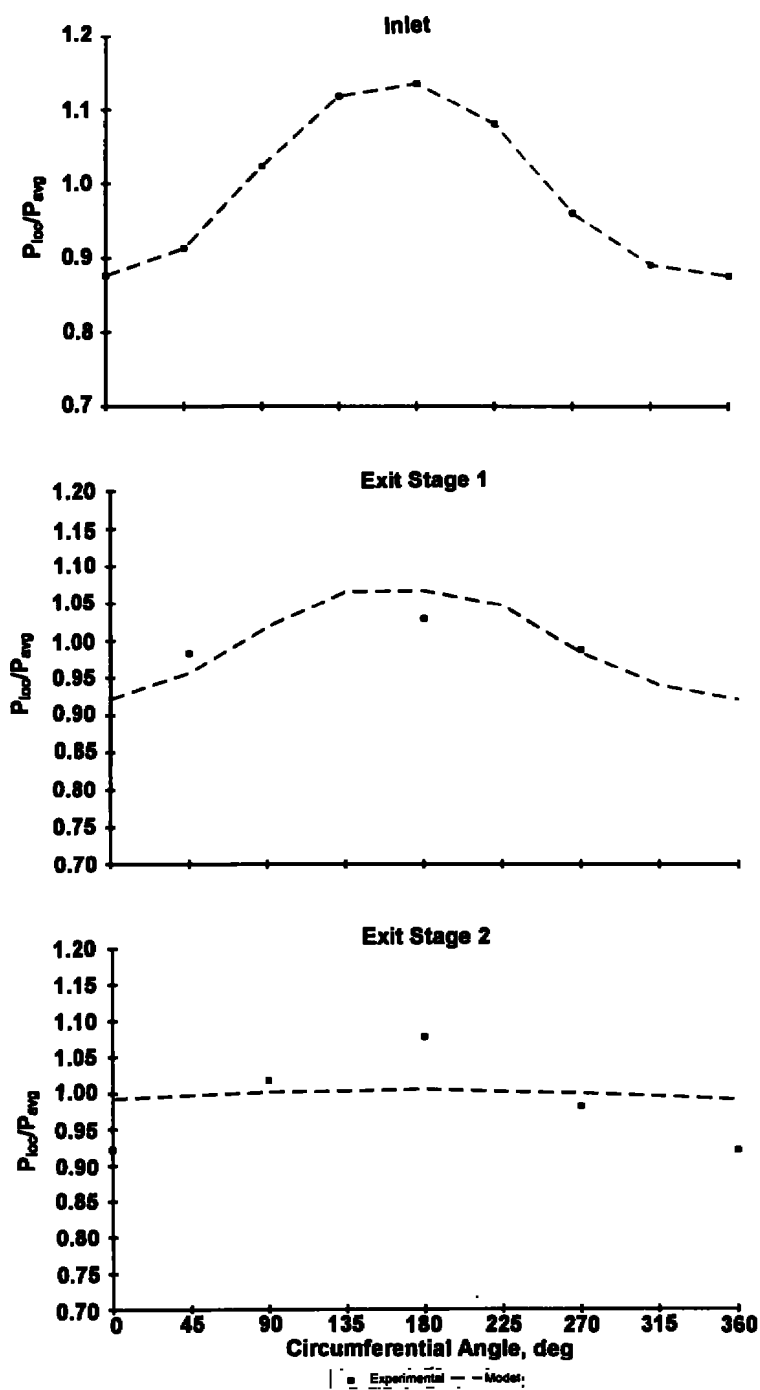


Figure 26. Compressor performance prediction for one/revolution circumferential distortion screen at 85-percent corrected rotor speed.

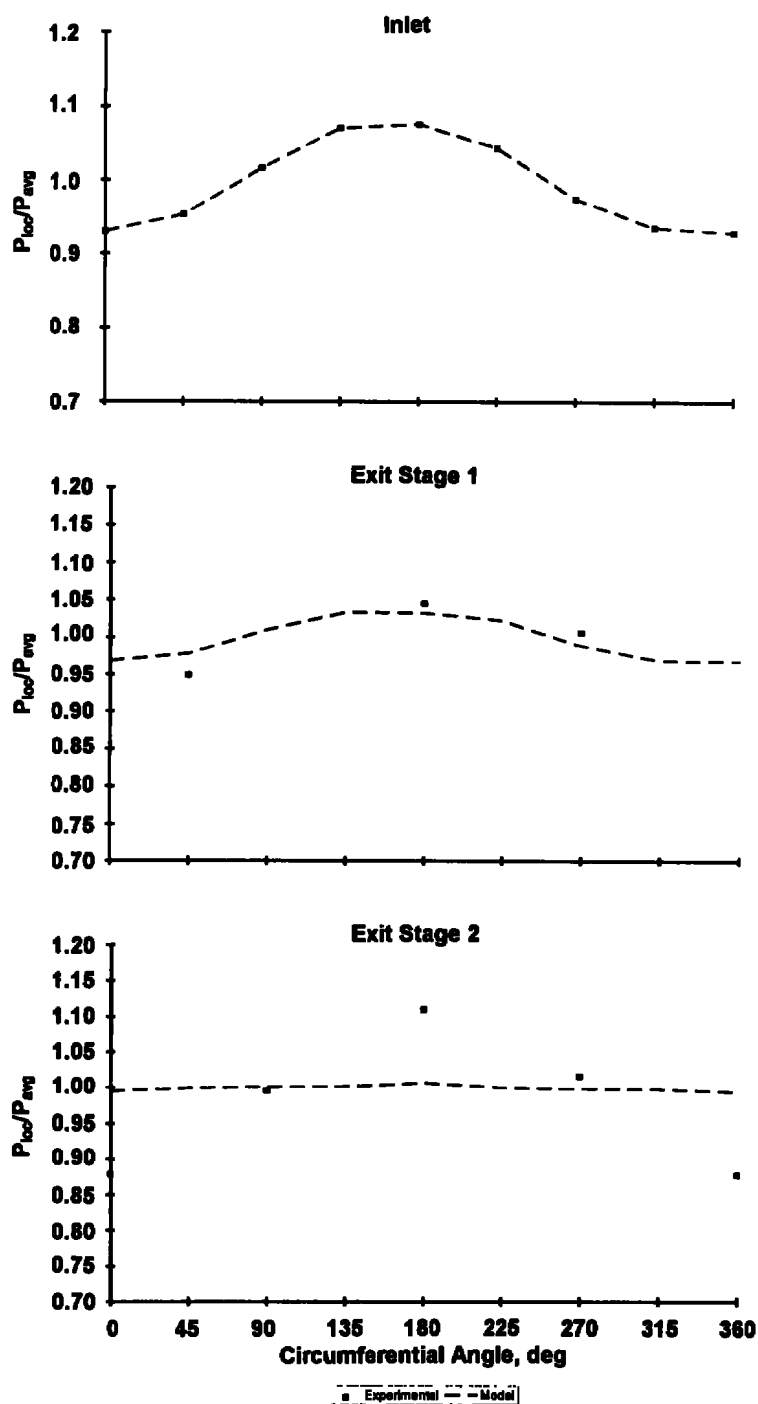


a. Near operating point

**Figure 27. Distortion attenuation for circumferential total pressure distortion at 98.6-percent corrected speed.**

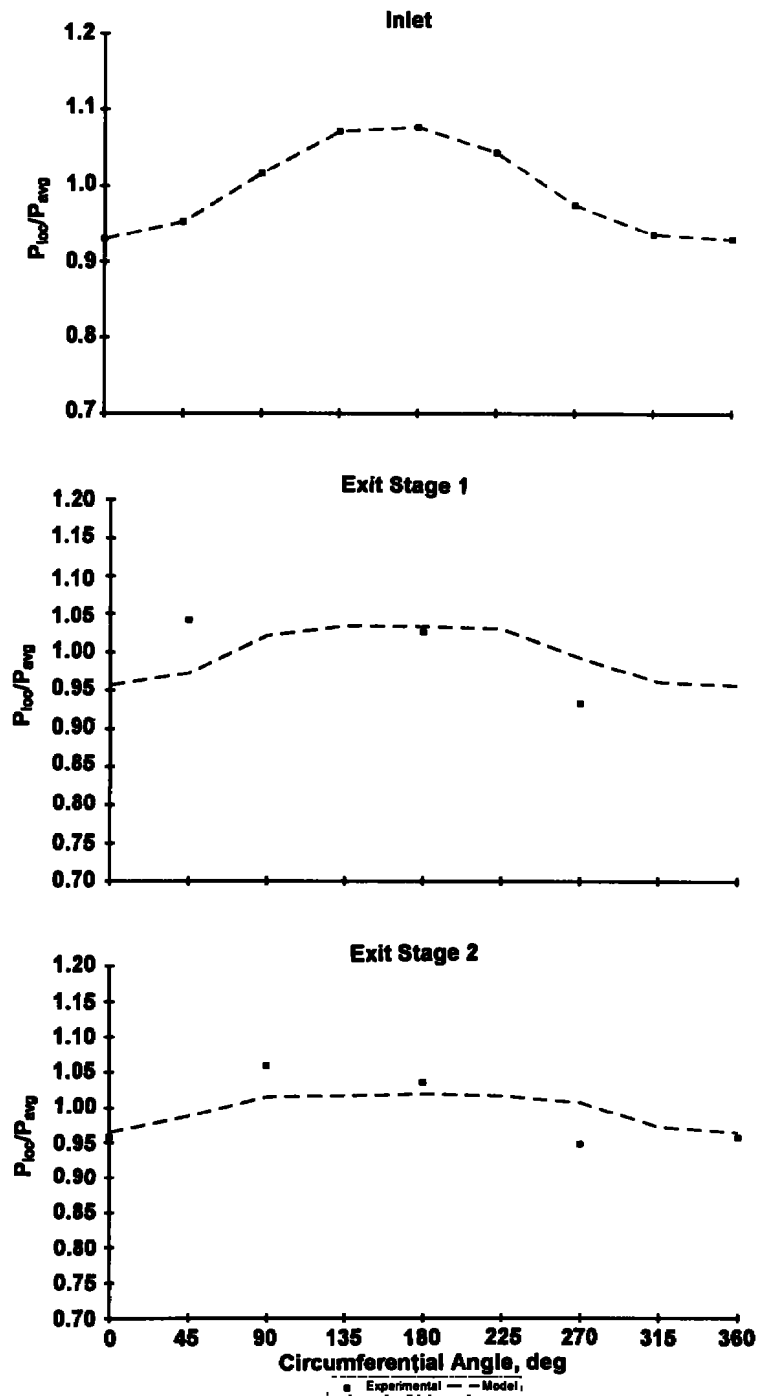


**b. Near stall point**  
**Figure 27. Concluded.**



a. Near operating point

**Figure 28. Distortion attenuation for circumferential total pressure distortion at 85-percent corrected speed.**



**b. Near stall point**  
**Figure 28. Concluded.**



**Distortion Inlet Total Pressure Contours  
Percent Deviation from Face Average (Interpolated)**

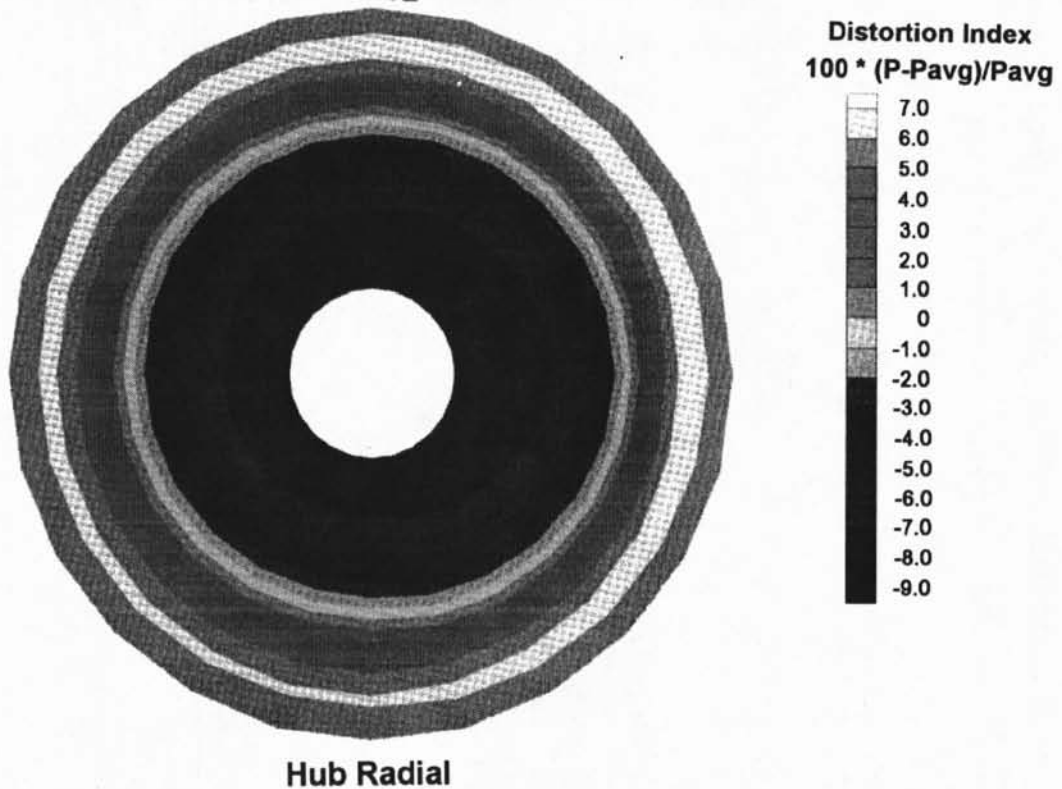


**Figure 29. Typical inlet total pressure pattern produced by a hub-radial distortion screen [Courtesy of Compressor Research Facility, Wright-Patterson Air Force Base].**

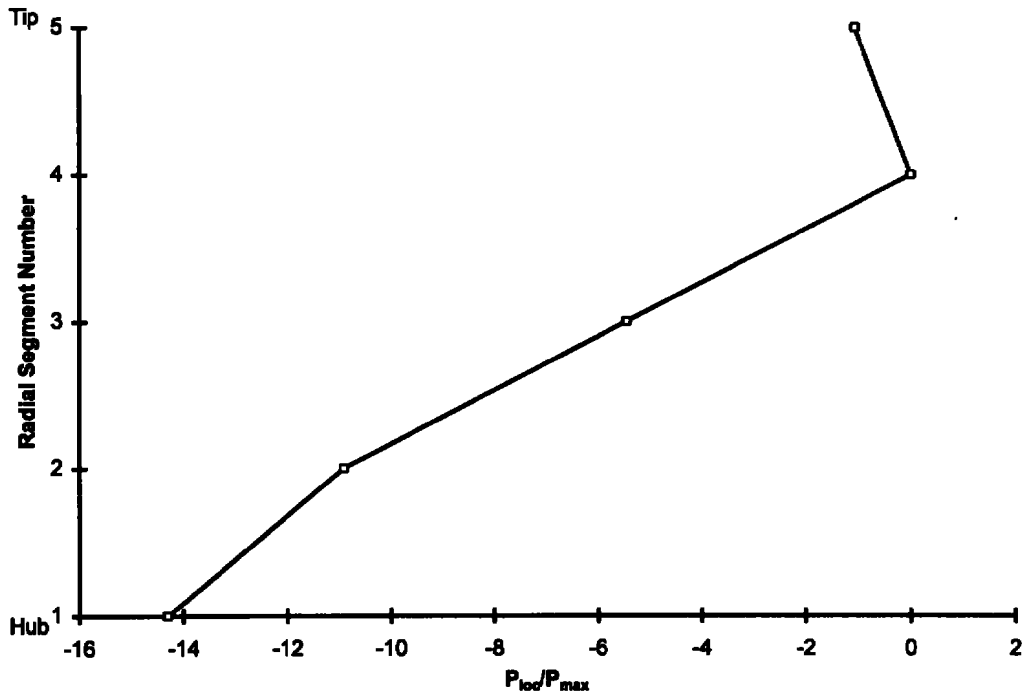


**Figure 30. Total pressure distortion pattern produced by a hub-radial distortion screen at 98.6-percent corrected rotor speed.**

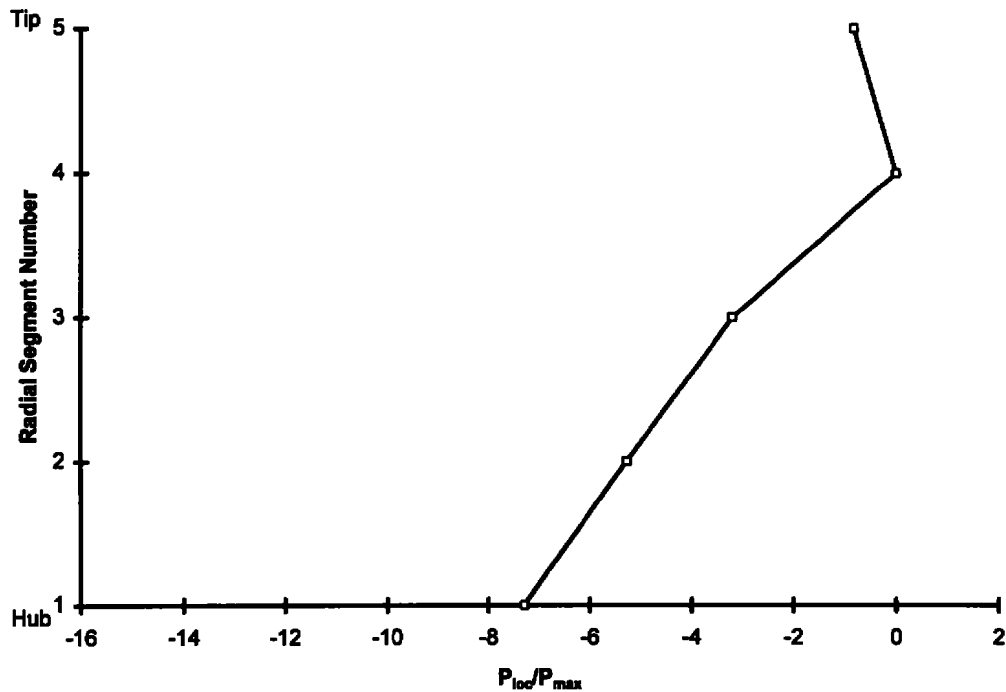


**Figure 31. Total pressure distortion pattern produced by a hub-radial distortion screen at 85-percent corrected rotor speed.**

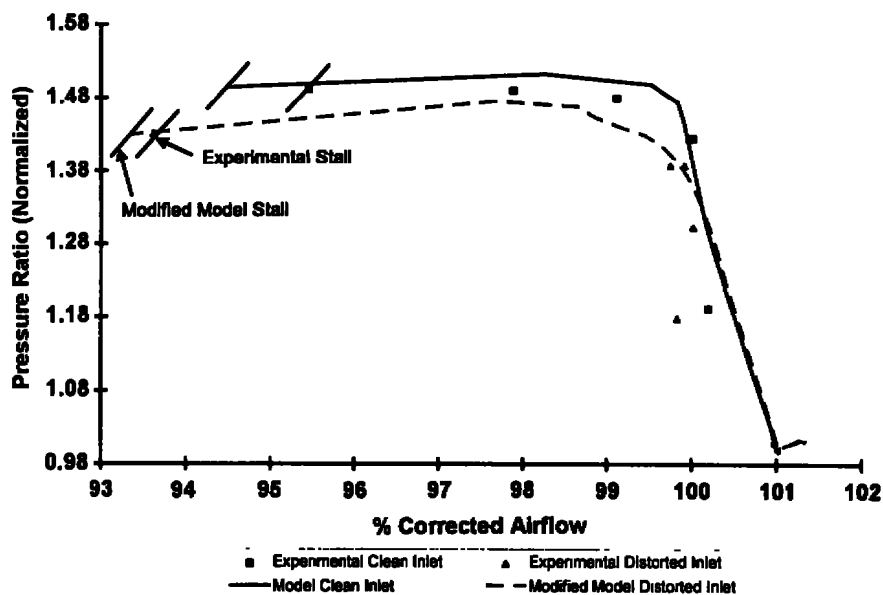


**Figure 32. Compressor performance prediction for hub-radial distortion screen at 98.6-percent corrected rotor speed.**

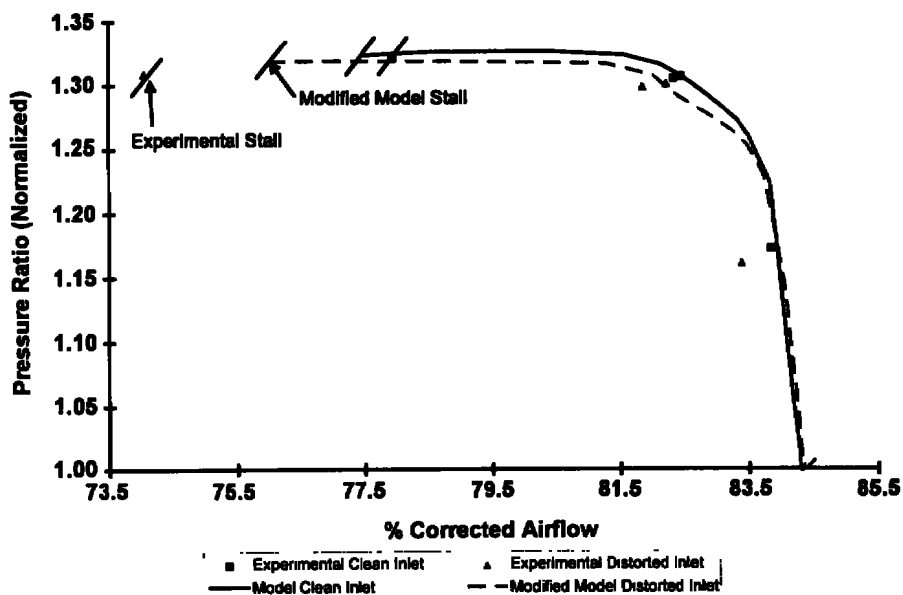
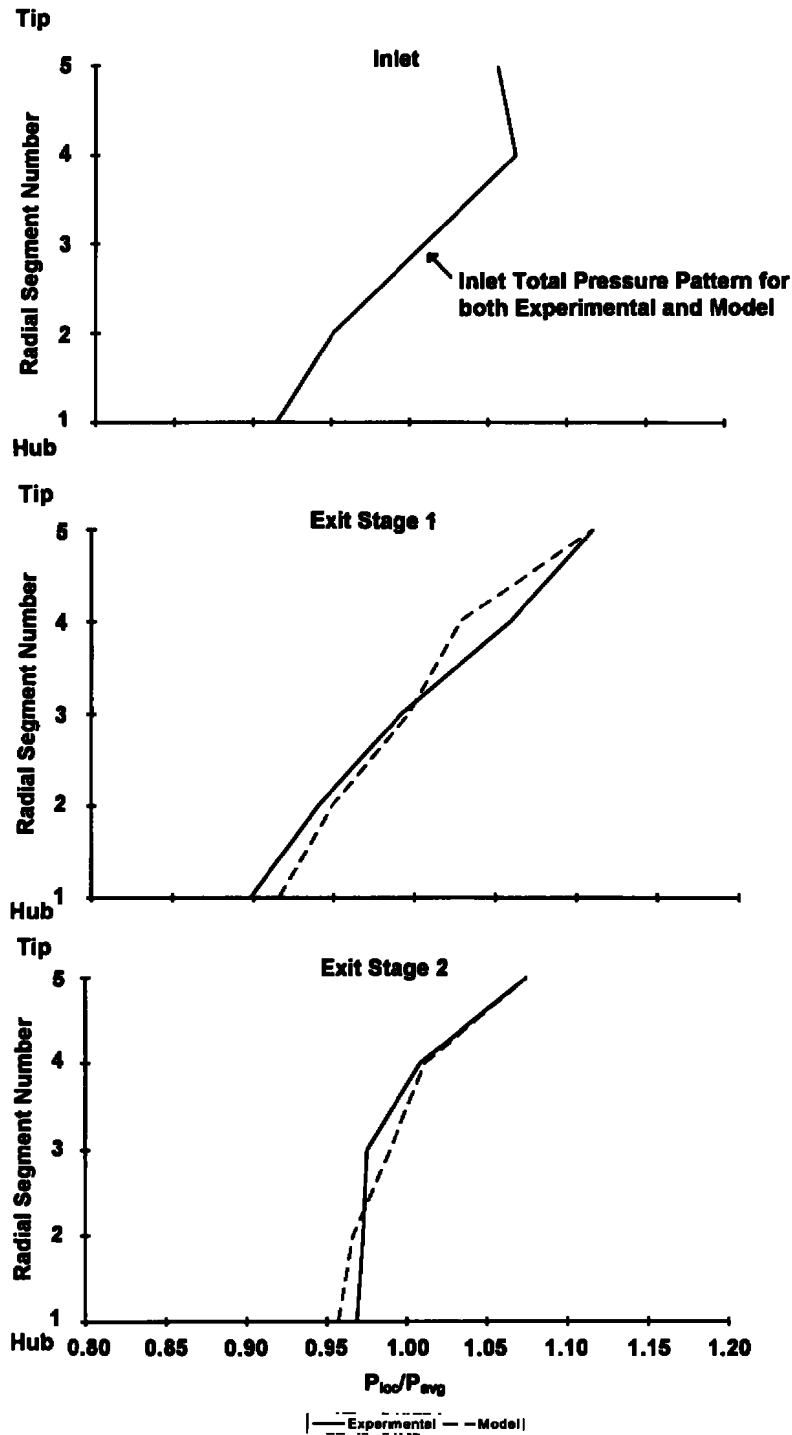
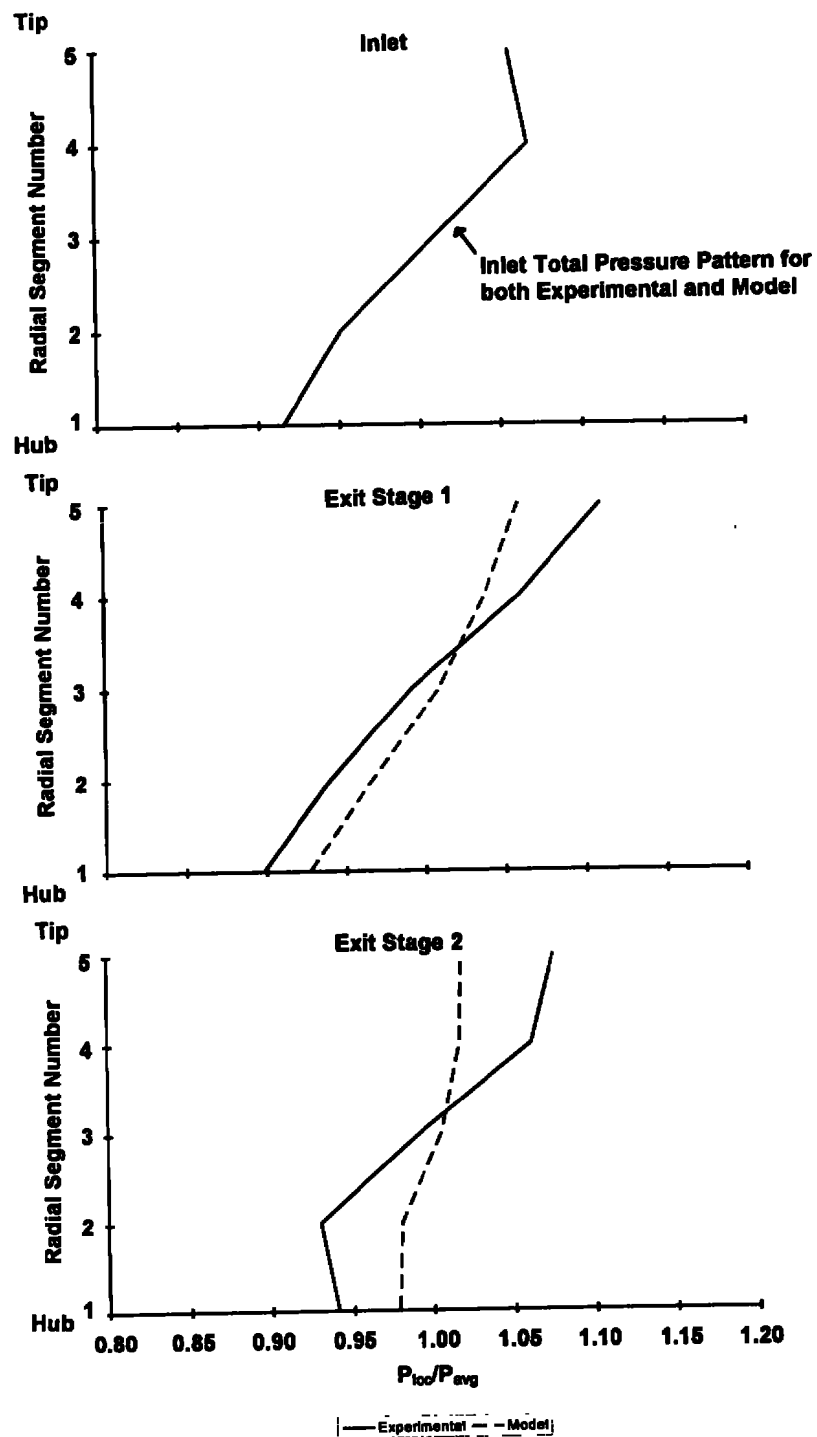


**Figure 33. Compressor performance prediction for hub-radial distortion screen at 85-percent corrected rotor speed.**

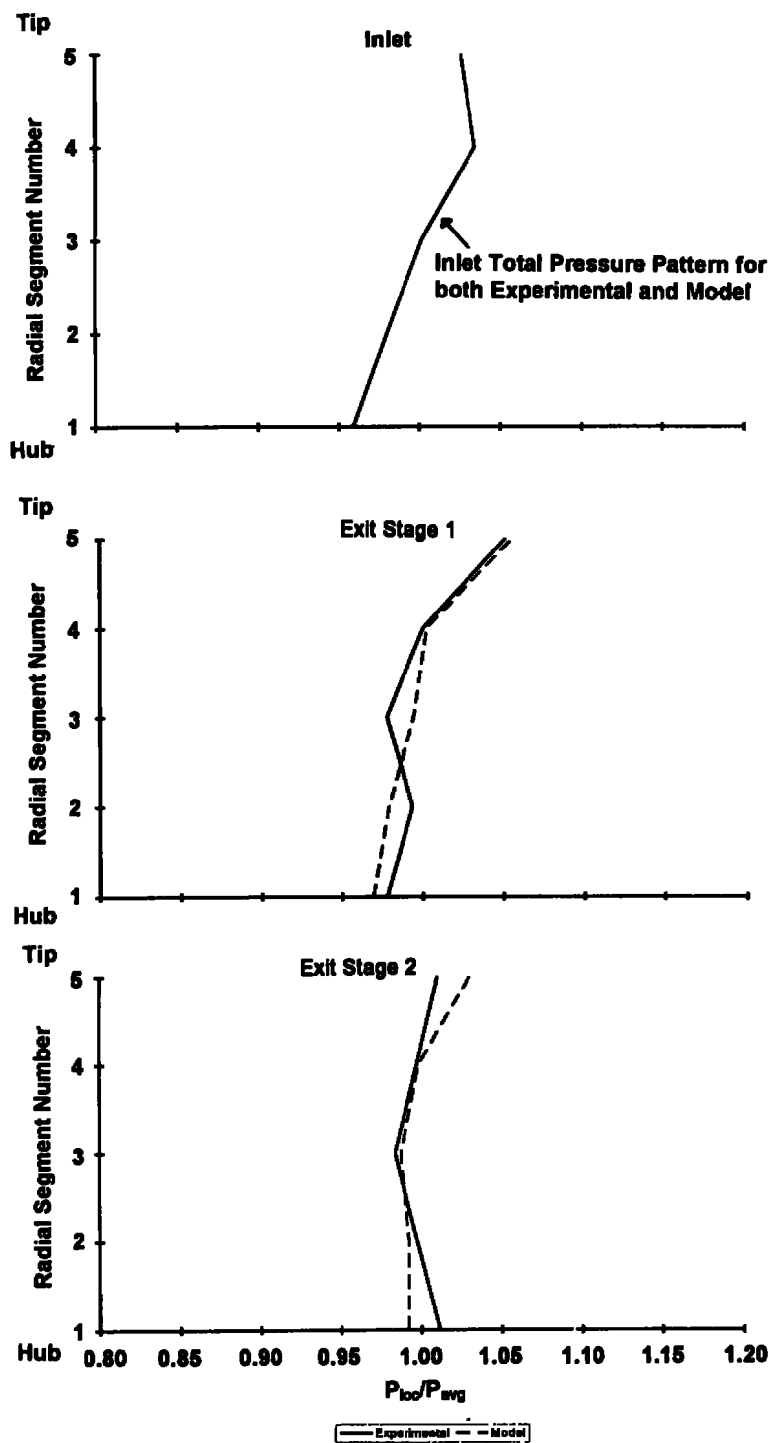


a. Near operating point

Figure 34. Distortion attenuation for hub-radial total pressure distortion at 98.6-percent corrected speed.

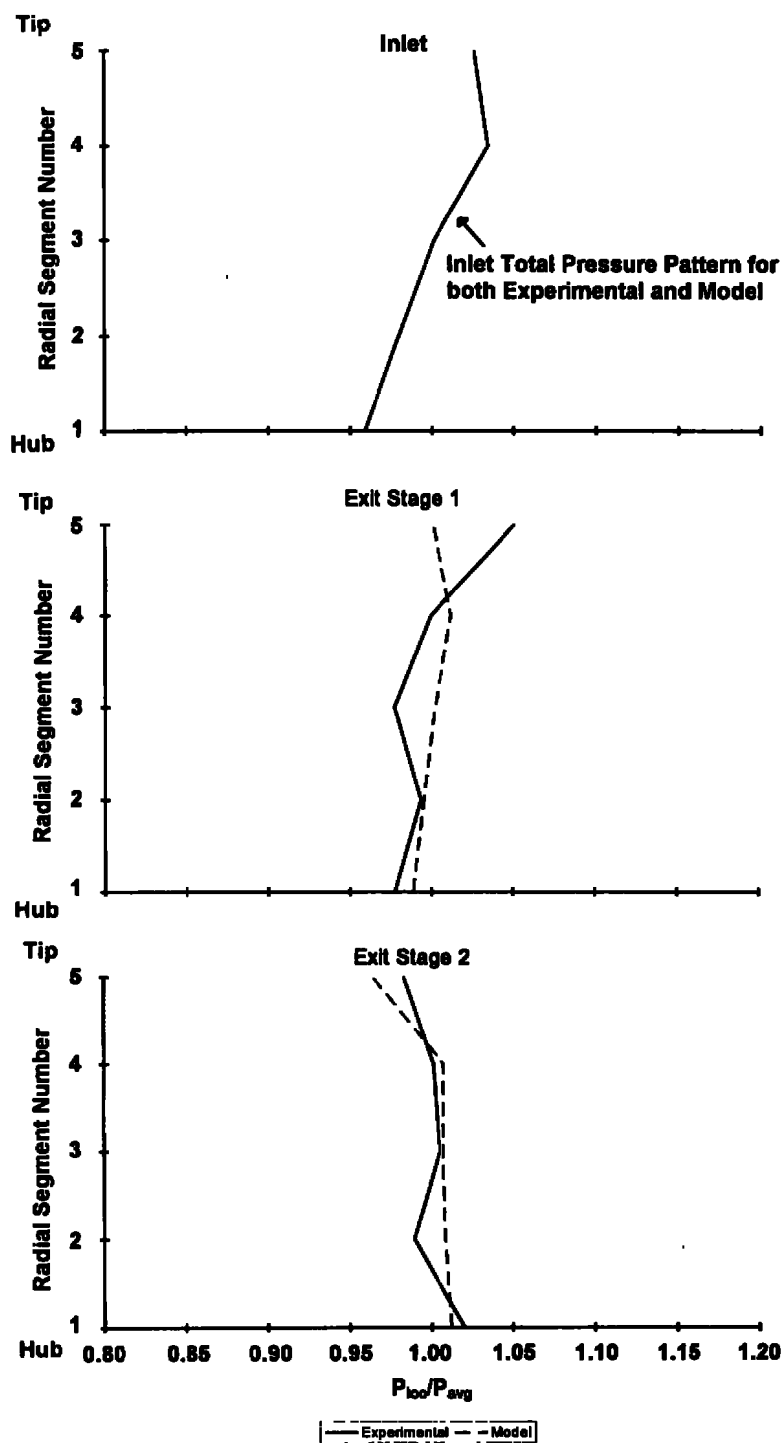


b. Near stall point  
Figure 34. Concluded.



a. Near operating point

Figure 35. Distortion attenuation for hub-radial total pressure distortion at 85-percent corrected speed.



b. Near stall point  
Figure 35. Concluded.

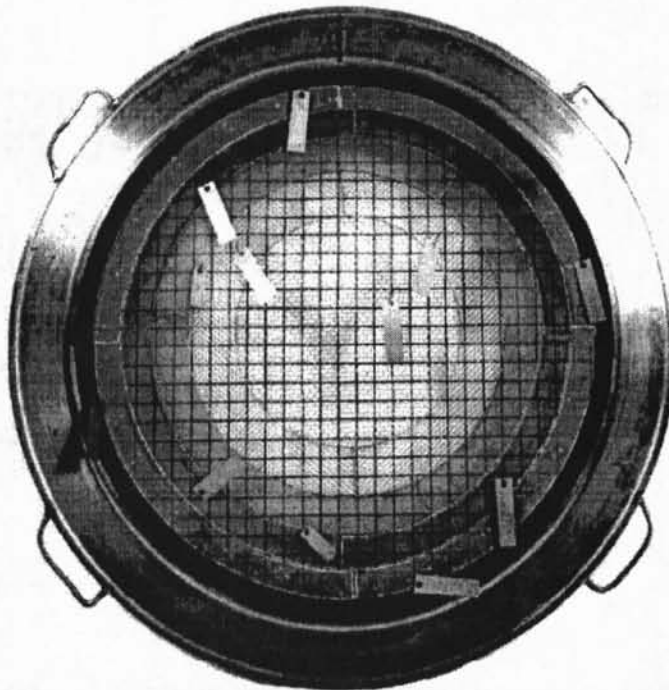


**Figure 36. Tip-radial total pressure distortion screen [Courtesy of the Compressor Research Facility, Wright-Patterson Air Force Base].**

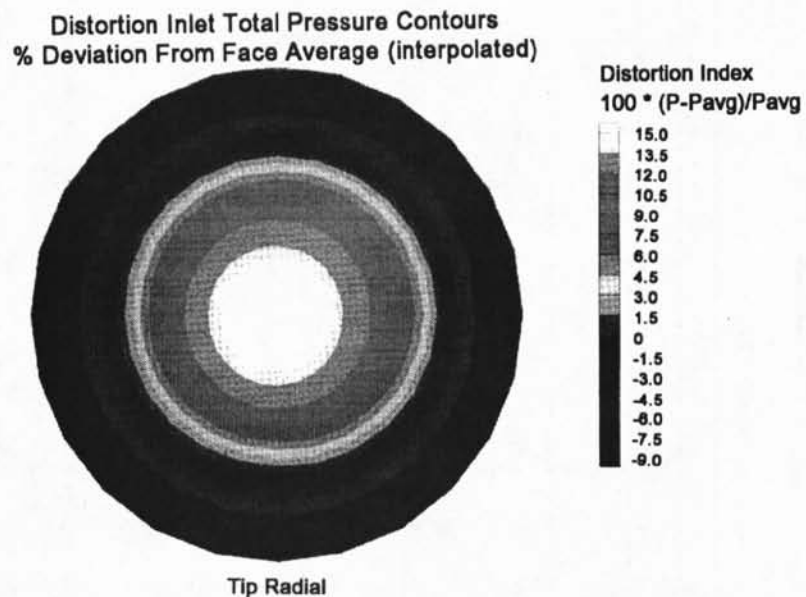


**Figure 37. Typical inlet total pressure pattern produced by a tip-radial distortion screen [Courtesy of the Compressor Research Facility, Wright-Patterson Air Force Base].**



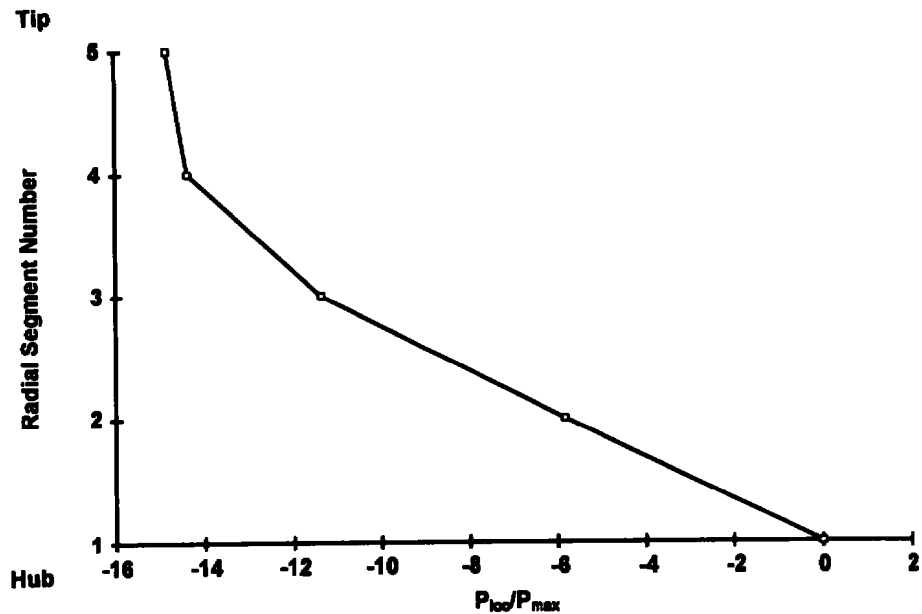


Figure 38. Total pressure distortion pattern produced by a tip-radial distortion screen at 85-percent corrected rotor speed.

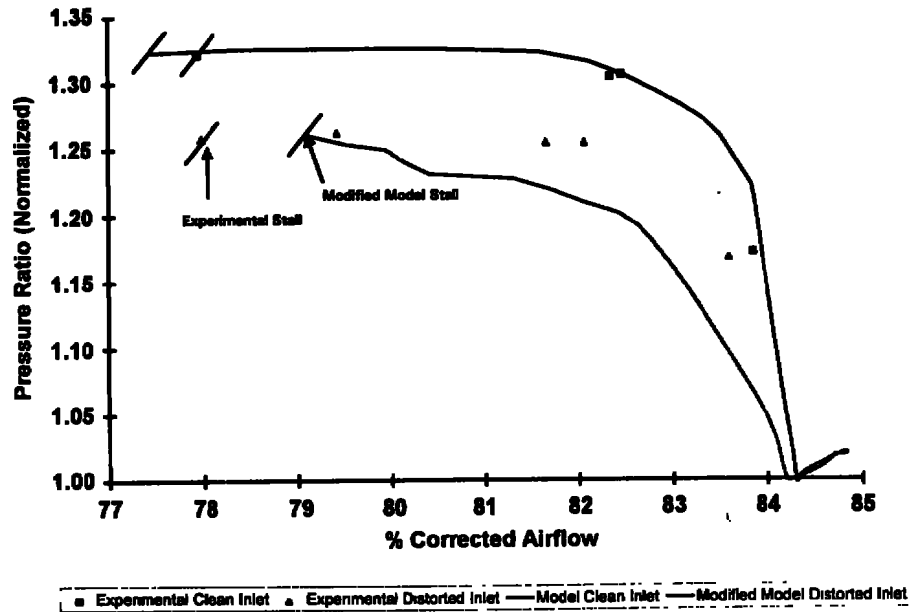
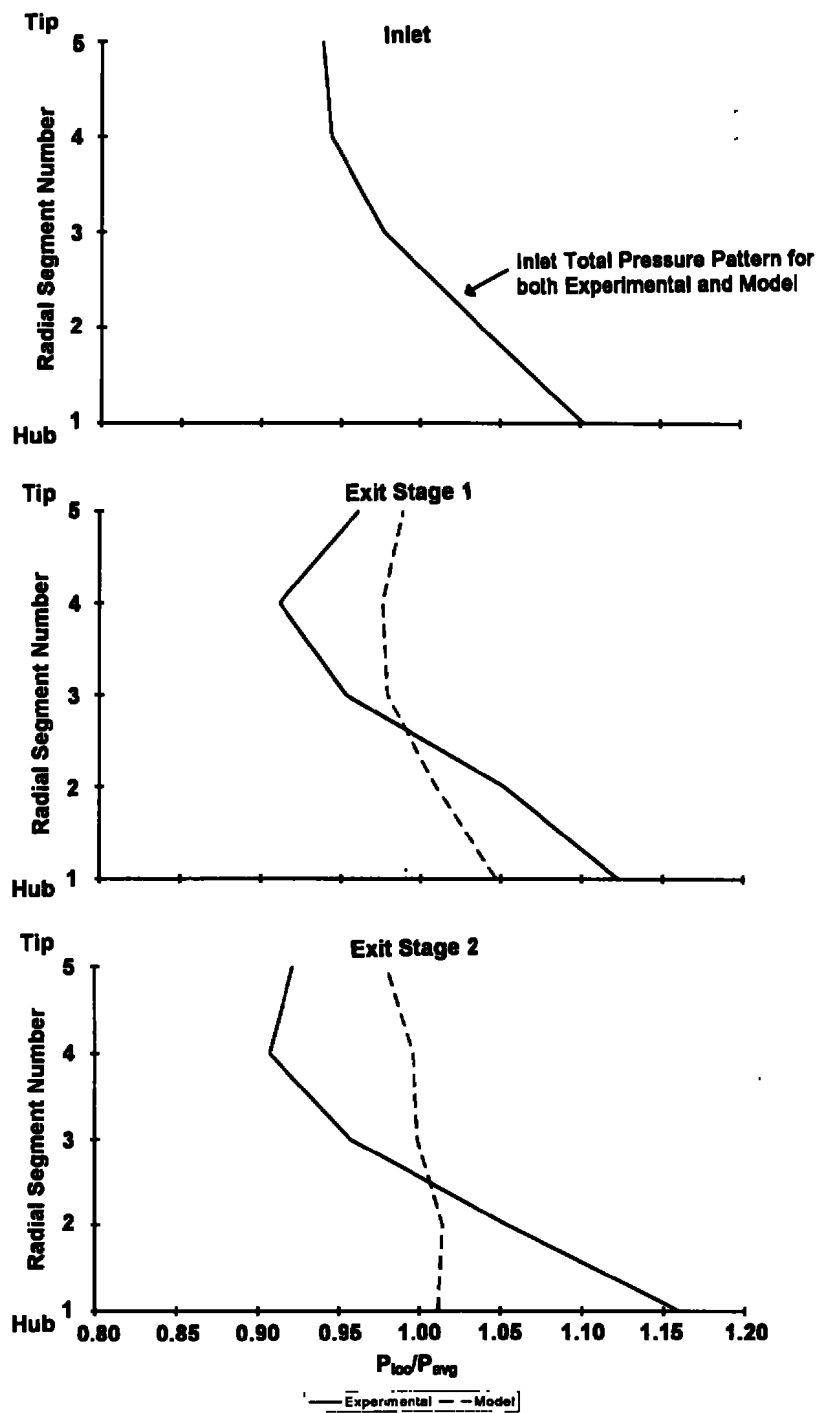
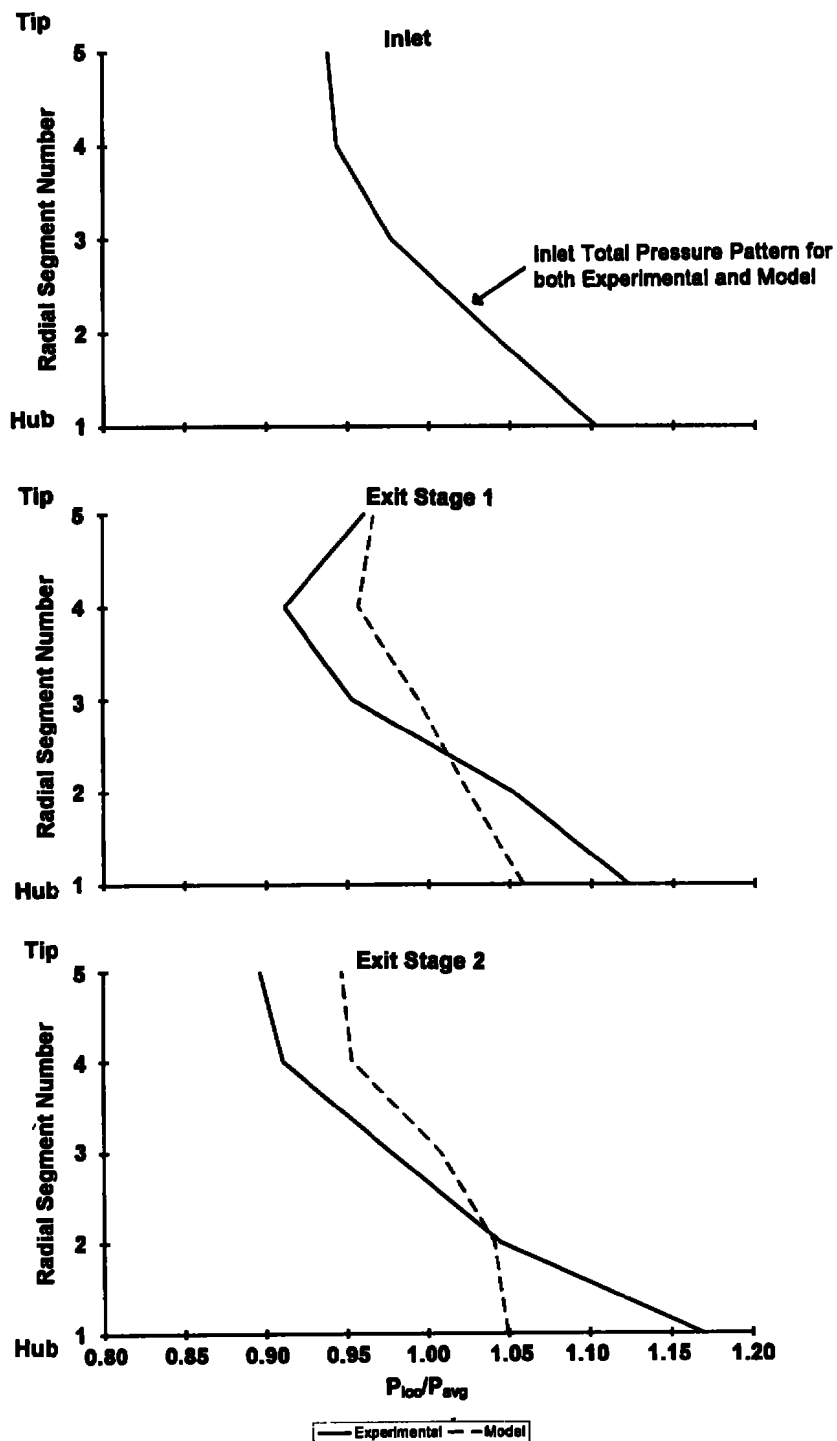


Figure 39. Compressor performance prediction for tip-radial distortion screen at 85-percent corrected rotor speed.



a. Near operating point

Figure 40. Distortion attenuation for hub-radial total pressure distortion at 85-percent corrected speed.



b. Near stall point  
Figure 40. Concluded.

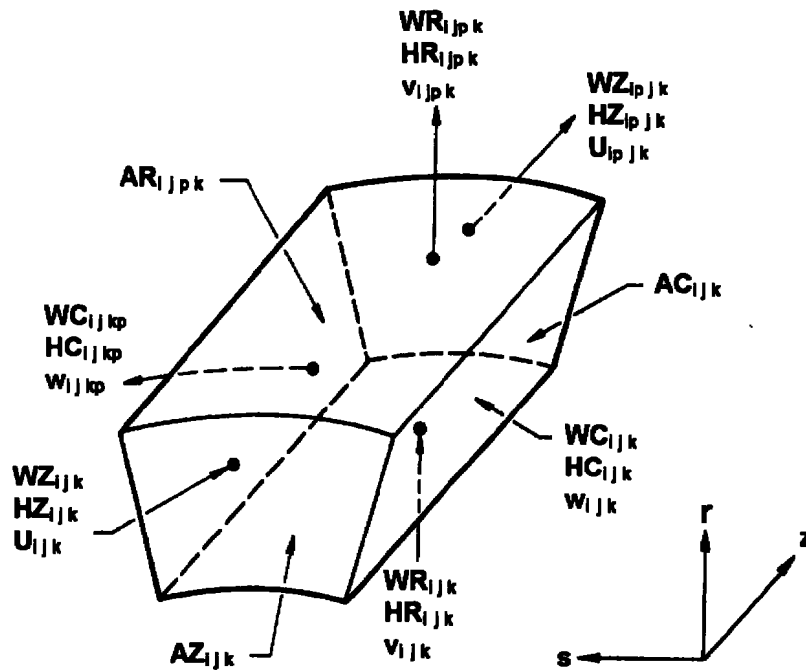


Figure 41. Three-dimensional control volume (Ref. 18).

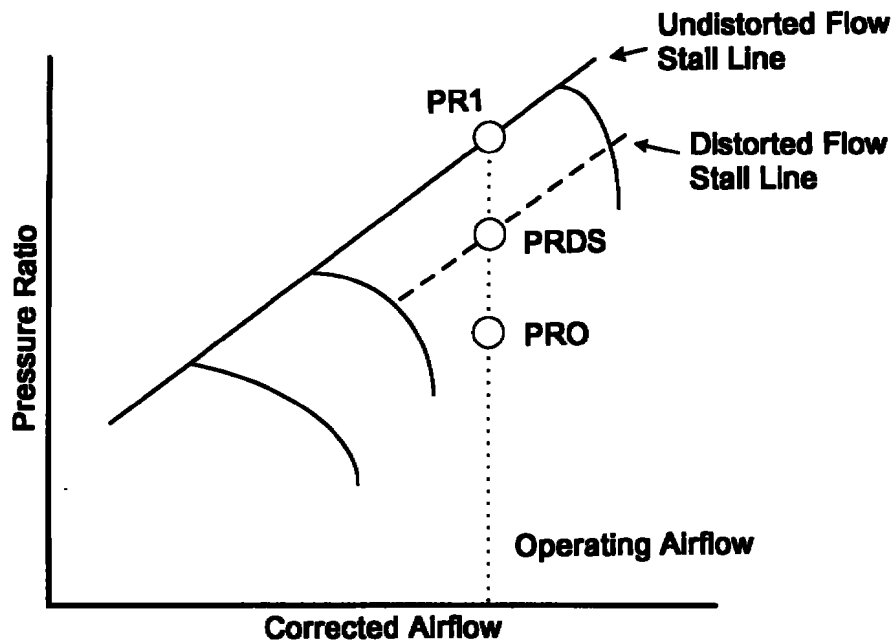


Figure 42. Illustration for stall margin calculations (Based on image from ARP 1420 standard, Ref. 15).

**Table 1. Comparison of Model Predicted Instability Point Versus Experimental Data (Clean Inlet at 98.6-Percent Speed)**

	Model	Experimental	Percent Difference
Percent $W_{corr}$	94.5	95.5	1.0
PR (normalized)	1.49	1.49	0.16

**Table 2. Comparison of Model Predicted Instability Point Versus Experimental Data (Clean Inlet at 85-Percent Speed)**

	Model	Experimental	Percent Difference
Percent $W_{corr}$	77.4	77.9	0.64
PR (normalized)	1.32	1.32	0.14

**Table 3. Summary of Stall Margin Calculations for Model and Experimental Data at Both Speeds with Clean Inlet**

Percent Corrected Rotor Speed	Stall Margin, SM		
	Model	Experimental	Percent Difference
98.6	34.2	32.4	5.6
85	24.1	22.9	4.9

**Table 4. Comparison of the Modified Model Predicted Instability Point Versus Experimental Data (One/Revolution Inlet Distortion Pattern at 98.6-Percent Speed)**

	Model	Experimental	Percent Difference
Percent $W_{corr}$	98.0	98.5	-0.44
PR (normalized)	1.33	1.36	-2.36

**Table 5. Comparison of the Modified Model Predicted Instability Point Versus Experimental Data (One/Revolution Inlet Distortion Pattern at 85-Percent Speed)**

	Model	Experimental	Percent Difference
Percent $W_{corr}$	75.6	75.7	-0.20
PR (normalized)	1.26	1.27	-1.43

**Table 6. Summary of Stall Calculations for Modified Model and Experimental Results (One/Revolution Inlet Distortion at 98.6-Percent Speed)**

	Model	Experimental
$SM_{Clean}$ Percent	33.46	33.62
$SM_{Dist}$ Percent	14.21	16.35
$\Delta SM$ Percent	19.25	17.27
$\Delta PRS$ Percent	14.42	12.93

**Table 7. Summary of Stall Calculations for Modified Model and Experimental Results (One/Revolution Inlet Distortion at 85-Percent Speed)**

	Model	Experimental
$SM_{Clean}$ Percent	21.26	21.36
$SM_{Dist}$ Percent	21.26	22.72
$\Delta SM$ Percent	-0.001	-1.72
$\Delta PRS$ Percent	-0.001	-1.36

**Table 8. Comparison of the Parallel Model Predicted Instability Point Versus Experimental Data (One/Revolution Inlet Distortion Pattern at 98.6-Percent Speed)**

	Model	Experimental	Percent Difference
Percent $W_{corr}$	99.4	98.5	0.96
PR (normalized)	1.35	1.36	0.86

**Table 9. Comparison of the Parallel Model Predicted Instability Point Versus Experimental Data (One/Revolution Inlet Distortion Pattern at 85-Percent Speed)**

	Model	Experimental	Percent Difference
Percent $W_{corr}$	82.3	75.7	8.63
PR (normalized)	1.26	1.27	1.19

**Table 10. Work Redistribution Scale Factors for Both the Pressure and Temperature Characteristics for the 98.6-Percent Corrected Speed**

Stage	Radial Segment	Pressure Scale Factors	Temperature Scale Factors
1	1	0.992	0.969
1	2	0.999	0.968
1	3	0.990	0.973
1	4	0.972	0.986
1	5	1.02	1.07
2	1	1.05	0.981
2	2	1.00	0.961
2	3	0.990	0.968
2	4	0.985	0.985
2	5	0.963	1.06

**Table 11. Work Redistribution Scale Factors for Both the Pressure and Temperature Characteristics for the 85-Percent Corrected Speed**

Stage	Radial Segment	Pressure Scale Factors	Temperature Scale Factors
1	1	1.02	0.980
1	2	1.00	0.976
1	3	0.983	0.978
1	4	0.969	0.988
1	5	1.00	1.05
2	1	1.03	0.978
2	2	1.01	0.963
2	3	1.01	0.964
2	4	1.01	1.00
2	5	0.958	1.06

**Table 12. Comparison of the Modified Model Predicted Instability Point Versus Experimental Data (Hub-Radial Inlet Distortion Pattern at 98.6-Percent Speed)**

	Model	Experimental	Percent Difference
Percent $W_{corr}$	93.3	93.6	-0.287
PR (normalized)	1.43	1.43	0.077

**Table 13. Comparison of the Modified Model Predicted Instability Point Versus Experimental Data (Hub-radial Inlet Distortion Pattern at 85-Percent Speed)**

	Model	Experimental	Percent Difference
Percent $W_{corr}$	76.0	74.1	2.67
PR (normalized)	1.32	1.31	-0.727



**Table 14. Summary of Stall Calculations for Modified Model and Experimental Results (Hub-Radial Inlet Distortion at 98.6-Percent Corrected Speed)**

	Model	Experimental
$SM_{Clean}$ Percent	31.48	31.60
$SM_{Dist}$ Percent	30.22	29.89
$\Delta SM$ Percent	1.26	1.71
$\Delta PRS$ Percent	0.965	1.30

**Table 15. Summary of Stall Calculations for Modified Model and Experimental Results (Hub-Radial Inlet Distortion at 85-Percent Corrected Speed)**

	Model	Experimental
$SM_{Clean}$ Percent	21.58	20.09
$SM_{Dist}$ Percent	26.37	29.52
$\Delta SM$ Percent	-4.79	-9.43
$\Delta PRS$ Percent	-3.94	-7.85

**Table 16. Comparison of the Modified Model Predicted Instability Point Versus Experimental Data (Tip-Radial Inlet Distortion Pattern at 85-Percent Speed)**

	Model	Experimental	Percent Difference
Percent $W_{corr}$	79.1	78.0	1.43
PR (normalized)	1.26	1.26	0.209

**Table 17. Summary of Stall Calculations for Modified Model and Experimental Results (Hub-Radial Inlet Distortion at 85-Percent Corrected Speed)**

	Model	Experimental
$SM_{Clean}$ Percent	23.71	22.96
$SM_{Dist}$ Percent	15.25	16.98
$\Delta SM$ Percent	8.46	5.98
$\Delta PRS$ Percent	6.84	4.86

## APPENDIX A GOVERNING EQUATIONS

### A.1.0 EQUATION SUBSCRIPT CONVENTION

The equation subscript convention is an indexing scheme based on the three-dimensional control volume shown in Fig. 41 (Ref. 10). The indices  $ijk$  document the three coordinates: axial, radial, and circumferential, respectively. For a term with the subscript  $ijk$ , it is referenced to the  $i$  axial plane, the  $j$  radial plane, and the  $k$  circumferential plane. To designate the next incremental plane, the term  $p$  is included in the subscript following the appropriate coordinate index. An example subscript would be  $ijpk$ , where the referenced location is the  $i$  axial plane, the  $j+1$  radial plane, and the  $k$  circumferential plane, respectively. Conversely, the term  $m$  in the subscript designates the previous incremental plane. Therefore, the  $ijkm$  subscript would reference the  $i$  axial plane, the  $j$  radial plane, and the  $k-1$  circumferential plane, respectively.

### A1.1 ONE-DIMENSIONAL GOVERNING EQUATIONS

The current research is based on Kimzey's research efforts (Ref. 10) and begins with a set of governing equations for the axial direction, including the continuity, momentum, and energy equations. The continuity equation for the axial direction is as follows,

$$\underbrace{W + \frac{\partial W}{\partial x} dx + WB dx}_{\text{mass leaving control volume per unit time}} + \underbrace{\frac{\partial (\rho A dx)}{\partial t}}_{\text{time rate of increase of mass "stored" in the control volume}} = \underbrace{W}_{\text{mass entering control volume per unit time}} \quad (\text{A-1})$$

which reduces to

$$\frac{\partial (\rho A)}{\partial t} = \frac{\partial W}{\partial x} - W_B \quad (\text{A-2})$$

For the axial momentum, the net change of momentum in the axial direction is equal to the sum of all the forces in the axial direction,

$$\underbrace{F dx + PSA - \left[ PSA + \frac{\partial(PSA)}{\partial x} dx \right] + PS \left[ \left( A + \frac{\partial A}{\partial x} dx \right) - A \right]}_{\text{axial forces acting on control volume}} =$$

$$\underbrace{\left[ \underbrace{WU + \frac{\partial(WU)}{\partial x} dx}_{\text{momentum leaving the control volume per unit time}} - \underbrace{WU}_{\text{momentum entering the control volume per unit time}} + \underbrace{\frac{\partial}{\partial t} [\rho U A dx]}_{\text{time rate of increase of momentum "stored" in the control volume}} \right]}_{\text{total time rate of change of momentum}} \quad (A-3)$$

which reduces to

$$\frac{\partial W}{\partial t} = \frac{\partial(IMP)}{\partial x} + F + PS \frac{\partial A}{\partial x} \quad (A-4)$$

The impulse function, IMP, is defined as

$$IMP = WU + PS A. \quad (A-5)$$

The energy equation shown below is presented in a form similar to the momentum equation.

$$\underbrace{H + \frac{\partial H}{\partial x} dx}_{\text{enthalpy leaving the control volume per unit time}} + \underbrace{\frac{\partial}{\partial t} \left[ \rho \left( e + \frac{U^2}{2} \right) A \right] dx}_{\text{time rate of increase of energy "stored" in the control volume}}$$

$$= \underbrace{H}_{\text{enthalpy entering the control volume per unit time}} + \underbrace{WS dx}_{\text{shaft work done on the fluid in the control volume}} + \underbrace{Q dx}_{\text{heat added to the fluid in the control volume}} \quad (A-6)$$

Equation (A-6) may be reduced to

$$\frac{\partial(XA)}{\partial t} = \frac{\partial H}{\partial x} + WS + Q \quad (A-7)$$

where the energy function, X, is

$$X = \rho \left[ e + \frac{U^2}{2} \right] \quad (A-8)$$

and the enthalpy,  $H$ , is defined as

$$H = c_p WT \quad (A-9)$$

Additional equations include the perfect-gas equation

$$PS = \rho R TS, \quad (A-10)$$

the relationships for internal energy and enthalpy

$$e = c_v TS + \text{constant} \quad (A-11)$$

$$h = c_p TS + \text{constant} \quad (A-12)$$

as well as the polytropic relations for total pressure and temperature

$$P = PS \left[ \frac{T}{TS} \right]^{\frac{\gamma}{\gamma-1}} \quad (A-13)$$

where

$$\gamma = \frac{c_p}{c_v} \quad (A-14)$$

and

$$T = c_p TS + \frac{U^2}{2} \quad (A-15)$$

The Mach number is also used and defined as

$$M = \frac{U}{a}. \quad (A-16)$$

where the acoustic velocity,  $a$ , is

$$a = \sqrt{\gamma RTS} = \sqrt{\gamma \frac{PS}{\rho}} \quad (A-17)$$

In terms of the Mach number and static pressure, the energy function,  $X$ , can be expressed as

$$X = \frac{PS}{\gamma - 1} \left[ 1 + \frac{\gamma(\gamma-1)}{2} M^2 \right] \quad (A-18)$$

by using Eqs. (A-8), (A-10), (A-11), (A-13), (A-16), and (A-17). The impulse function, IMP, can also be expressed in a Mach number/static pressure form.

$$IMP = PS A [1 + \gamma M^2] \quad (A-19)$$

## A1.2 THREE-DIMENSIONAL GOVERNING EQUATIONS

The previous section discussed the governing equations for a one-dimensional model. The next step is to discuss the governing equations in terms of a three-dimensionally distorted flow, based on Kimzey's derivations (Ref. 10). Now the radial and circumferential directions must be accounted for along with the axial.

Begin by assuming that the control volume can be approximated by a volume that is rectangular on all faces (Fig. 41). The governing equation for mass continuity for this control volume can be described as follows.

$$\underbrace{WZ_{ijk} + WR_{ijk} + WC_{ijk}}_{\text{mass flow entering the control volume per unit time}} + \underbrace{WZ_{ipjk} + WR_{ijpk} + WC_{ijkp}}_{\text{mass flow leaving the control volume per unit time}} + \underbrace{\frac{\partial}{\partial t} \int_{vol_{ijk}} \rho d(vol)}_{\text{time rate of increase of mass "stored" in the control volume}} \quad (A-20)$$

where  $WZ_{ijk}$ ,  $WR_{ijk}$ , and  $WC_{ijk}$  are the mass flows across the axial, radial, and circumferential surfaces of the control volume.

The momentum equations for the axial, circumferential, and radial directions are similar in form to the continuity equation presented above. For the axial direction, the axial momentum equation is the same as that presented in the previous section, but is now in more general terms.

$$\underbrace{[FZ_{ijk} + \overline{PS_{ijk}ARZ_{ijk}} + \overline{PS_{ijpk}ARZ_{ijpk}} + PS_{ijk}AZ_{ijk} - PS_{ipjk}AZ_{ipjk}]}_{\text{axial forces acting on the control volume}} \\ = \underbrace{WZ_{ipjk}U_{ipjk} + \overline{WR_{ijpk}U_{ijpk}} + \overline{WC_{ijkp}U_{ijkp}}}_{\text{axial momentum leaving the control volume per unit time}}$$

$$\begin{aligned}
 & - \underbrace{\overline{WZ_{ijk}U_{ijk}} - \left( \overline{-WR_{ijk}U_{ijk}} \right) - \overline{WC_{ijp}U_{ijp}}}_{\text{axial momentum entering the control volume per unit time}} \\
 & + \underbrace{\frac{\partial}{\partial t} \int_{vol_{ijk}} (\rho U) d(vol)}_{\text{time rate of increase of axial momentum "stored" in the control volume}}
 \end{aligned} \tag{A-21}$$

In the above equation, the force term FZ includes the blading and casing forces acting on the fluid. The area terms used follow the projected area convention. For example, the area term ARZ is the area of the axial surface (Z) of the radially facing surface (R). The barred terms used in Eq. (50) represent surface integrals. An example is the integration of a pressure across a control volume surface shown below.

$$\overline{PS_{ijk}ARZ_{ijk}} = \int_{ARZ_{ijk}} PS d(ARZ) \tag{A-22}$$

The circumferential momentum equation follows a form similar to that of the axial, where the circumferential force term, FC, includes Coriolis and viscous forces.

$$\begin{aligned}
 & \underbrace{FC_{ijk} + \overline{PS_{ijk}ACC_{ijk}} - \overline{PS_{ipjk}ACC_{ipjk}}}_{\text{circumferential forces acting on the control volume}} \\
 & = \underbrace{\overline{WZ_{ipjk}w_{ipjk}} + \overline{WR_{ijpk}w_{ijpk}} + \overline{WC_{ijkp}w_{ijkp}}}_{\text{circumferential momentum leaving the control volume per unit time}} \\
 & - \underbrace{\overline{WZ_{ijk}w_{ijk}} - \overline{WR_{ijk}w_{ijk}} - \overline{WC_{ijk}w_{ijk}}}_{\text{circumferential momentum entering the control volume per unit time}} \\
 & + \underbrace{\frac{\partial}{\partial t} \int_{vol_{ijk}} (\rho w) d(vol)}_{\text{time rate of increase of circumferential momentum "stored" in the control volume}}
 \end{aligned} \tag{A-23}$$

The radial momentum equation also follows a similar form, where the radial force term, FR, includes centrifugal and viscous forces.

$$\begin{aligned}
 & \underbrace{[FR_{ijk} + \overline{PS_{ijk}ACR_{ijk}} + \overline{PS_{ijkp}ACR_{ijkp}} + \overline{PS_{ijk}ARR_{ijk}} - \overline{PS_{ijkp}ARR_{ijkp}}]}_{\text{radial forces acting on control volume}} \quad (A-24) \\
 & = \underbrace{\overline{WZ_{ipjk}v_{ipjk}} + \overline{WR_{ipk}v_{ipk}} + \overline{WC_{ijkp}v_{ijkp}}}_{\text{radial momentum leaving the control volume per unit time}} \\
 & - \underbrace{\overline{WZ_{ijk}v_{ijk}} - \overline{WR_{ijk}v_{ijk}} - \overline{WC_{ijk}v_{ijk}}}_{\text{radial momentum entering the control volume per unit time}} \\
 & + \underbrace{\frac{\partial}{\partial t} \int_{vol_{ijk}} (\rho v) d(vol)}_{\text{time rate of increase of radial momentum "stored" in the control volume}}
 \end{aligned}$$

The energy equation for the control volume, Eq. (54), has a form similar to the momentum equations.

$$\begin{aligned}
 & \underbrace{\overline{HZ_{ijk}} + \overline{HR_{ijk}} + \overline{HC_{ijk}}}_{\text{enthalpy entering the control volume per unit time}} + \underbrace{\overline{WS + Q}}_{\text{shaft work done and heat added to the fluid in the control volume per unit time}} \quad (A-25) \\
 & = \underbrace{\overline{WZ_{ipjk}} + \overline{HR_{ipk}} + \overline{HC_{ijkp}}}_{\text{enthalpy leaving the control volume per unit time}} + \underbrace{\frac{\partial}{\partial t} \int_{vol_{ijk}} \rho \left[ e + \frac{U^2 + v^2 + w^2}{2} \right] d(vol)}_{\text{time rate of increase of energy "stored" in the control volume}}
 \end{aligned}$$



## APPENDIX B

### STALL MARGIN CALCULATIONS

The stall margin calculations are based on the ARP 1420 standard (Ref. 15). For the clean inlet case, the calculations are simply the stall margin. For the inlet distortion cases, the calculations include the clean flow stall margin, distorted flow stall margin, the change in stall margin, and the loss in stall pressure rise (See Fig. 42). The stall calculations are summarized below.

Undistorted stall margin:

$$SM_{clean} = \frac{(PR1-PR0)}{PR0} * 100 \quad (B-1)$$

Distorted flow stall margin:

$$SM_{dist} = \frac{(PRDS-PR0)}{PR0} * 100 \quad (B-2)$$

Change in stall pressure rise:

$$\Delta PRS = \frac{(PR1-PRDS)}{PR1} * 100 \quad (B-3)$$

Change in stall margin:

$$\Delta SM = \frac{PR1}{PR0} * \Delta PRS \quad (B-4)$$

## NOMENCLATURE

<b>a</b>	Acoustic velocity
<b>A</b>	Area
<b>C</b>	Orifice discharge coefficient; Chord
<b><math>C_l</math></b>	Coefficient of lift
<b><math>c_p</math></b>	Constant pressure specific heat
<b><math>c_v</math></b>	Constant volume specific heat
<b>D</b>	Diameter
<b>DC</b>	Distortion index
<b>DLR</b>	Dynamic lag ratio
<b>e</b>	Internal energy
<b>F</b>	Force
<b>FR</b>	Radial force term
<b>f</b>	Frequency
<b>g</b>	Gravitational constant
<b>H, h</b>	Enthalpy
<b>IMP</b>	Impulse function
<b>K</b>	Orifice flow coefficient
<b>k</b>	Reduced frequency
<b>M</b>	Mach number
<b>N</b>	Rotor rotational velocity
<b>P</b>	Pressure
<b>PR</b>	Pressure ratio
<b><math>\Delta PRS</math></b>	Percent change in overall pressure ratio at stall
<b>PS</b>	Static pressure
<b>Q</b>	Heat transfer rate
<b>r</b>	Radius
<b>S</b>	Shaft work
<b>SM</b>	Stall margin, percent
<b><math>\Delta SM</math></b>	Change in stall margin
<b>t</b>	Time
<b>T</b>	Temperature
<b>U</b>	Axial velocity
<b>v</b>	Radial velocity
<b>v</b>	Specific volume
<b>V</b>	Velocity components other than axial
<b>W</b>	Mass flow rate
<b>WC</b>	Mass flow rate in the circumferential direction

<b>WR</b>	Mass flow rate in the radial direction
<b>%W</b>	Mass flow rate as a percent of design
<b>w</b>	Circumferential velocity
<b>x</b>	Axial coordinate
<b>X</b>	Energy function
<b>z</b>	Vertical distance
<b><math>\Phi, \phi</math></b>	Compressor flow coefficient
<b><math>\psi</math></b>	Compressor stage loading parameter
<b><math>\alpha</math></b>	Angle of attack
<b><math>\beta</math></b>	Orifice geometric parameter
<b><math>\epsilon</math></b>	Cascade geometry parameter
<b><math>\rho</math></b>	Fluid density
<b><math>\gamma</math></b>	Ratio of specific heats
<b><math>\theta</math></b>	Angle
<b><math>\lambda</math></b>	Stagger angle
<b><math>\omega</math></b>	Rotation speed

### Subscripts

<b>1</b>	Station or location 1
<b>2</b>	Station or location 2
<b>avg</b>	Average
<b>B</b>	Bleed
<b>c</b>	Circumferential coordinate
<b>Clean</b>	Clean or uniform total pressure inlet condition
<b>corr</b>	Corrected
<b>crit</b>	Critical
<b>Dist</b>	Distorted inlet total pressure condition
<b>gap</b>	Distance between the compressor rotor and stator
<b>HIGH</b>	Upper or larger region relative to surrounding areas (e.g., $PS_{HIGH}$ — high static pressure region)
<b>LOW</b>	Lower or smaller region relative to surrounding areas (e.g., $PS_{LOW}$ — low static pressure region)
<b>max</b>	Maximum
<b>min</b>	Minimum
<b>net</b>	Difference between two flux terms
<b>R; r</b>	Radial coordinate
<b>ref</b>	Reference
<b>rel</b>	Relative

<b>ss</b>	<b>Steady state</b>
<b>t</b>	<b>Total or stagnation; throat (e.g., orifice "throat")</b>
<b>T</b>	<b>Total</b>
<b>x</b>	<b>Axial direction</b>
<b><math>\theta</math></b>	<b>Tangential</b>